

THE DISTRIBUTION AND MAGNITUDE OF EROSION OVER MILLENNIAL
TIMESCALES AT ENGABREEN, NORWAY

AN ABSTRACT

SUBMITTED ON THE THIRD DAY OF MAY, 2019

TO THE DEPARTMENT OF EARTH AND ENVIRONMENTAL SCIENCES

IN PARTIAL FULFILLMENT OF THE REQUIREMENTS

OF THE SCHOOL OF SCIENCE AND ENGINEERING

OF TULANE UNIVERSITY

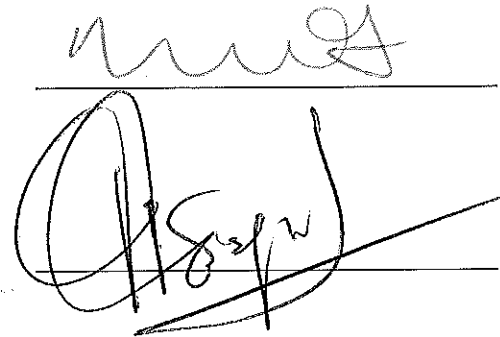
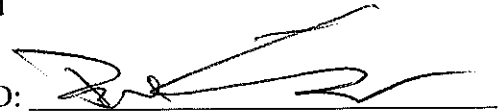
FOR

BY



Cari Rand

APPROVED:



ABSTRACT

We present estimates of Holocene glacial cover and subglacial erosion rates from Engabreen, a temperate glacier in coastal northern Norway, that indicate that the current forefield of the glacier was buried for a total of approximately 1,000 years during the Holocene. Erosion rates along two transects perpendicular to glacier flow are highly variable, ranging 0.24 – 4.36 mm yr⁻¹. We derive these estimates from in situ cosmogenic nuclide inventories, specifically those of ¹⁴C and ¹⁰Be, in bedrock exposed recently by the retreating Engabreen. In situ cosmogenic nuclide concentrations show no dependence on distance down or across the valley, leading us to conclude that decreased nuclide concentrations in rocks relative to others with a shared exposure history are indicative of spatially variable erosion.

Muons produce ¹⁴C at higher rates than ¹⁰Be and produce both nuclides at greater depths than do spallation reactions, so the ¹⁴C-¹⁰Be concentration ratio increases with depth. The production rates of these nuclides by muons are less than spallation production rates, however, so nuclide ratios generated by production at depth can be rapidly overprinted by surface production rates. ¹⁴C-¹⁰Be ratios elevated above the production ratio in samples of abraded bedrock indicates that sampled sites were deeply quarried during recent cover and then rapidly abraded prior to glacial retreat. This study shows ways that physical and chemical aspects of glacial landforms can reveal not just the modes of subglacial erosion that created them but also the locations and relative timing of specific erosional events.

THE DISTRIBUTION AND MAGNITUDE OF EROSION OVER MILLENNIAL
TIMESCALES AT ENGABREEN, NORWAY

A THESIS

SUBMITTED ON THE THIRD DAY OF MAY, 2019

TO THE DEPARTMENT OF EARTH AND ENVIRONMENTAL SCIENCES

IN PARTIAL FULFILLMENT OF THE REQUIREMENTS

OF THE SCHOOL OF SCIENCE AND ENGINEERING

OF TULANE UNIVERSITY

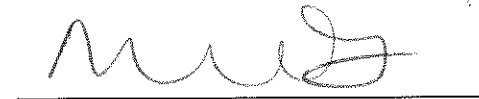
FOR

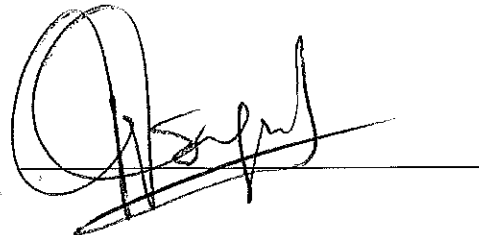
BY



Cari Rand

APPROVED: 





ACKNOWLEDGEMENTS

I wish to acknowledge the Purdue Rare Isotope Measurement laboratory, the Woods Hole National Ocean Sciences Accelerator Mass Spectrometry facility, and the University of California, Davis Stable Isotope Facility for sample nuclide measurements. I also wish to thank Drs. Brent M. Goehring, Nicole M. Gasparini, and Torbjörn E. Törnqvist for their guidance and reviews, which have greatly improved this document. I wish to extend my gratitude to my family, friends, and classmates for their support.

TABLE OF CONTENTS

ACKNOWLEDGMENTS i

LIST OF TABLES iii

LIST OF FIGURES iv

CHAPTERS

1. INTRODUCTION AND STUDY SITE 1

2. THE DISTRIBUTION AND MAGNITUDE OF EROSION OVER
MILLENNIAL TIMESCALES AT ENGABREEN, NORWAY 17

APPENDICES

A. SAMPLE IMAGES..... 52

B. LABORATORY METHODS..... 59

C. BAYESIAN ISOCHRON-FITTING METHODS..... 61

D. GEOCHEMICAL DATA TABLES 64

REFERENCES..... 66

LIST OF TABLES

2.1	Sample locations and parameters	33
2.2	Cosmogenic nuclide concentrations and apparent exposure ages	35
2.3	Calculated erosion depths and rates and ^{14}C - ^{10}Be concentration ratios..	38
A.1	Sample Images	54
D.1	^{14}C Sample Geochemical Data.....	64
D.2	^{10}Be Sample Geochemical Data.....	65

LIST OF FIGURES

1.1	Erosion rates from selected studies over the timeframes they examined.....	3
1.2	Schematic diagram of the accumulation, decay, and erosion of cosmogenic nuclides.....	7
1.3	Regional and local maps	11
1.4	Engabreen forefield orthophotographs draped on a digital terrain model	12
1.5	Comparison of historical and current photographs of Engabreen terminus ..	14
1.6	LiDAR data	16
2.1	^{10}B - 10^4C isochron	28
2.2	Sampling transect elevation profiles with nuclide concentrations.....	36
2.3	Exposure duration probability density function	37
2.4	Erosion depth error histograms.....	39
2.5	Joint exposure duration - beta probability density function contour plots....	40
2.6	Striation trend and foliation strike and dip data.....	42
2.7	Holocene marine limit map	44
2.8	^{14}C - ^{10}Be ratios versus depth	45
2.9	Sampling transect elevation profiles and erosion depths	47
2.10	Calculated sliding velocity by location and erosion depth by calculated sliding velocity	48
2.11	Lal-Klein-Nishiizumi C-Be plots.....	49
2.12	^{14}C production profiles	50
A.1	Upper transect, eastward view	52
A.2	Lower transect plucked face	52

A.3	EG10-03 plucked face and glacial striae.....	53
A.4	EG10-06 crescentic gouge.....	53
A.5	Upper transect striated surfaces, southward view.....	53

The Distribution and Magnitude of Erosion over Millennial Timescales at Engabreen, Norway

Chapter 1: Introduction and Study Site

1.1 Introduction

Coastal glaciers across eastern Norway retreated asynchronously following the Pleistocene and generally remained contracted for much of the middle and late Holocene, extending again as the Little Ice Age (LIA) began (Nesje, 2009). Even though glaciers are limited in spatial extent and confined to high elevations or latitudes, they can be efficient erosive agents capable of drastically altering the landscapes they cover (Koppes *et al.*, 2015). In this thesis, I use in situ produced cosmogenic radiocarbon (^{14}C) and beryllium-10 (^{10}Be) techniques to derive both the integrated duration of expanded and retracted ice cover at Engabreen in northern Norway and the mean glacial erosion rates experienced along two sample transects. Our results yield further insights into the processes occurring at the bed of the glacier through the measurement of average glacial erosion rates.

1.2 Motivation

Samples of actively-eroding subglacial bedrock are difficult to collect due to the challenges involved in accessing the beds of glaciers, particularly the overburden of thick, shifting ice and remoteness of glacial regions. Assigning a quantitative value to the rate at which bed material is removed by erosion can be arduous and often relies upon proxy data rather than direct measurement (see Hallet *et al.*, 1996 and references therein),

which hinders the study of the evolution of glacial landscapes. Better constraints on the magnitude of subglacial erosion will aid in modeling the history of glacial and post-glacial areas and better understanding the spatial distribution of erosion underneath glaciers will improve interpretations of the forms created by glacial erosion. Many related fields such as geomorphology and paleoclimatology make use of glacial erosion rate data, but this data is not available for all time periods nor is it evenly distributed geographically (Balco, 2011). Enhancing the global database of glacial erosion rates aids not just glaciologists but geomorphologists and others as well.

Glaciers are dynamic moving bodies of ice whose properties (such as size, thicknesses, and speed) change over time although, in many cases, we are limited to determining only average or integrated values for these parameters. Glaciers and the ice sheets from which they flow can also cover vast areas. Measurements taken in one area may therefore be dependent on conditions in other parts of the region or even world (Davis *et al.*, 2009) so filling in spatial gaps in the record can improve the interpretation of the data. Both long-term and short-term climatic trends exert powerful influence over the size and extent of glaciers and changing glacial size in turn affects the processes taking place within the ice and at the glacial bed. Different subglacial processes occur over different timescales and intervals as well, so it is important to understand over what timescales different effects may be accurately averaged (Fig. 1.1). Understanding the chain of factors that influence the action of ice on rock is vital to properly reconstructing past glacial landscapes.

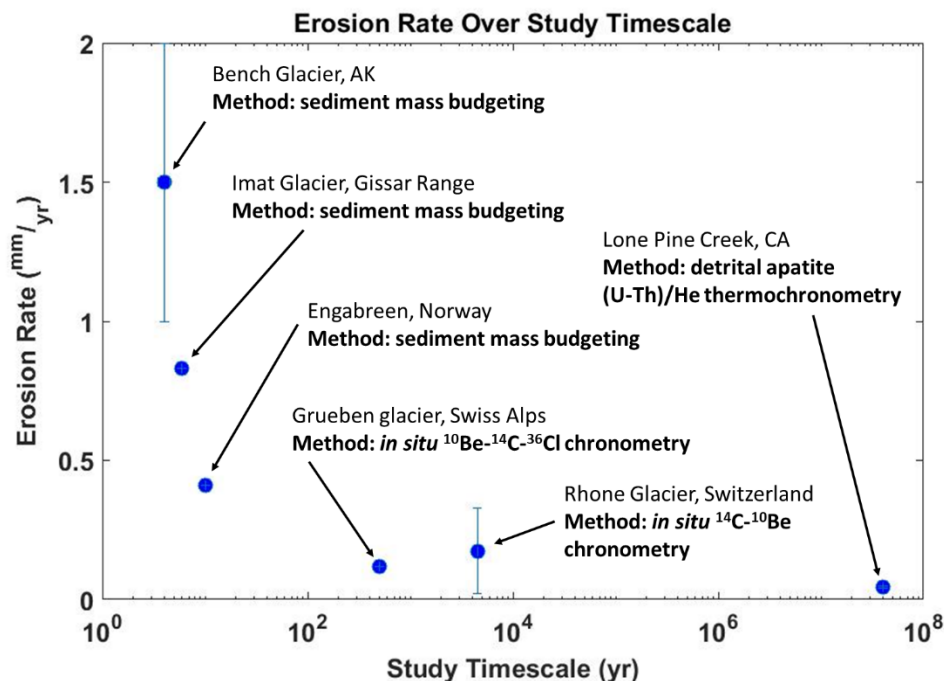


Figure 1.1. Erosion rates from selected studies over the timeframes they examined. This figure demonstrates the Sadler effect, in which measured rates of discontinuous phenomena show a dependence on the measurement interval. Note that this figure is neither comprehensive nor does it capture all of the factors which could influence the erosion rate of a glacier – for example, the Rhone Glacier study only sampled visibly-abraded surfaces, and the climate in which a glacier is located strongly affects how erosive it can be as well.

1.3 Background

1.3.1 Glacial Erosion

The action of glaciers sliding over their substrates can be quite erosive, leaving evidence of their passing in the scoured, polished, and plucked landscape and depositing moraines and other kinds of glacial deposits tracing the boundaries of their former extents. The positions and elevations of moraines serve as proxies for past temperature and precipitation in glaciated areas. A deteriorating climate and/or more snowfall will cause glaciers to gain mass and expand, building terminal moraines further downhill.

Inferring the conditions present during periods of reduced ice extent is more difficult, as subsequent glacial advances can destroy previously deposited moraines. While the total force a given glacier can exert depends on its mass and velocity, the total amount of that force that can be put towards erosion is more difficult to calculate. Glaciers can move by both basal sliding and internal deformation, but only sliding exerts sufficient force on the bed to cause significant abrasion (Martini *et al.*, 2001). The ideal model of glacial flow predicts that drag from valley sides will cause the velocity profile transverse to flow across a glacier to have a peak in the middle and minima on the sides. The Glen-Nye Flow law formulates it as such:

$$v_0 - v = \frac{K}{n+1} \sin^n \alpha * d^{n+1}, \quad (1.1)$$

in which v_0 refers to the velocity at the centerline of the glacier, v to the velocity at a given distance d from the centerline, and α to the slope of the bed surface. $K = \left(\frac{\rho g}{B}\right)^n$, in which ρ is the density of the ice, g the acceleration due to gravity, B a viscosity constant, and n an empirical constant that varies but is often in the vicinity of 3 (Nye, 1952). It is important to note that the centerline is not always the deepest part of the glacier. This equation can also be used to calculate a velocity profile with depth in a glacier by defining v_0 as the velocity at the surface of the glacier and v to the velocity at a given depth d in the glacier.

Bed conditions also strongly affect subglacial erosion rates. Bedrock clasts entrained by basal ice or meltwater drive subglacial abrasion processes, so variation in their hardness, size, and roundness as well as in the hardness and geometry of the substrate can affect subglacial abrasion rates (Beaud *et al.*, 2016). Ice thickness and basal water

pressure each exert control over the normal force at the bed, which affects how much pressure can be applied to the bed by a tool embedded in the basal ice (Hallet, 1981). A different erosive process, plucking, involves the sudden quarrying of whole blocks of bedrock from the valley floor. Plucking occurs when changes in subglacial water pressure focus transient stresses onto bedrock “steps”, taking advantage of preglacial joints and causing subcritical cracks to grow (Hooyer *et al.*, 2012). This is far more dependent on the local geometry and drainage conditions of the bed and may behave independently of the larger scale geometry of the valley (Anderson, 2014). Plucking processes also depend on subglacial water pressure and favorable topography to focus subglacial forces enough to quarry large blocks, so even small-scale changes in the mass balance of glaciers can change their erosivity by altering the subglacial hydrology or raising the basal ice above or lowering it below its pressure melting point (Hallet, 1979; Rothlisberger and Iken, 1981; Hooyer *et al.*, 2012; Anderson, 2014).

The rheology, weathering, and structure of bedrock affect its susceptibility to erosion. Closely-spaced fractures and steep bed slopes, for example, can make a bedrock surface more susceptible to erosion by plucking (Hooyer *et al.*, 2012; Anderson, 2014), and the presence of sediments can armor the bed, preventing plucking and limiting abrasion (Beaud *et al.*, 2016). Subglacial water flows can also erode channels down into the rock of a glacier bed (Clayton *et al.*, 1999). These channels are termed Nye-channels to differentiate them from Röthlisberger-channels, which form by melting upwards into glacier ice (Martini *et al.*, 2001).

1.3.2 *Cosmogenic Nuclides*

Cosmic rays (high-energy particles emitted by stars and other high-energy astronomical phenomena) constantly bombard the Earth. When these particles interact with matter, they can induce nuclear reactions that break nuclei apart in a process known as spallation. The remains of these reactions are called in situ cosmogenic nuclides because the nuclides of interest are produced in situ within the mineral lattice. Almost all primary cosmic rays (those in space that have not yet interacted with our atmosphere) are charged and are thus affected by the magnetic field of the Earth, meaning that they are more likely to interact with matter on Earth at the high latitudes at which the magnetic inclination is greater and cutoff rigidity is lesser. They are also attenuated by the matter through which they pass, making the production rate of cosmogenic nuclides in a target dependent on atmospheric pressure and the mass of any overlying material. The degree to which a given type of cosmic ray is attenuated by matter is known as the “attenuation length” and is reported as a mass depth (g cm^{-2}). In other words, the attenuation length of a cosmic ray is the distance it will travel through a material of a given density (g cm^{-3}) before the ray has a $1/e$ chance of not having struck another atom (in the case of a particle beam, the attenuation length is the distance traveled before the intensity of the beam has decayed by a factor of $1/e$, roughly a 64% decrease). Spallation reactions produce nuclides in bedrock at depth of up to ~5 m, while muons can produce nuclides to below 100 m depth in bedrock, although nuclide production decreases exponentially with depth in both cases. Measuring cosmogenic nuclide concentrations can therefore reveal the amount of time a sample has spent at a certain depth. Functionally, we measure how long a given sample has been exposed at the surface of the Earth (Balco, 2011). Different production pathways also produce given nuclides at different rates. Complicating matters

further, the attenuation of the rate of production of a given nuclide with depth also depends on the pathway producing the nuclide (Fig. 1.2). Cosmogenic nuclide production can be represented as the sum of a set of exponentials, each representing a specific production pathway (Gosse and Phillips, 2001). Inverting modeled production

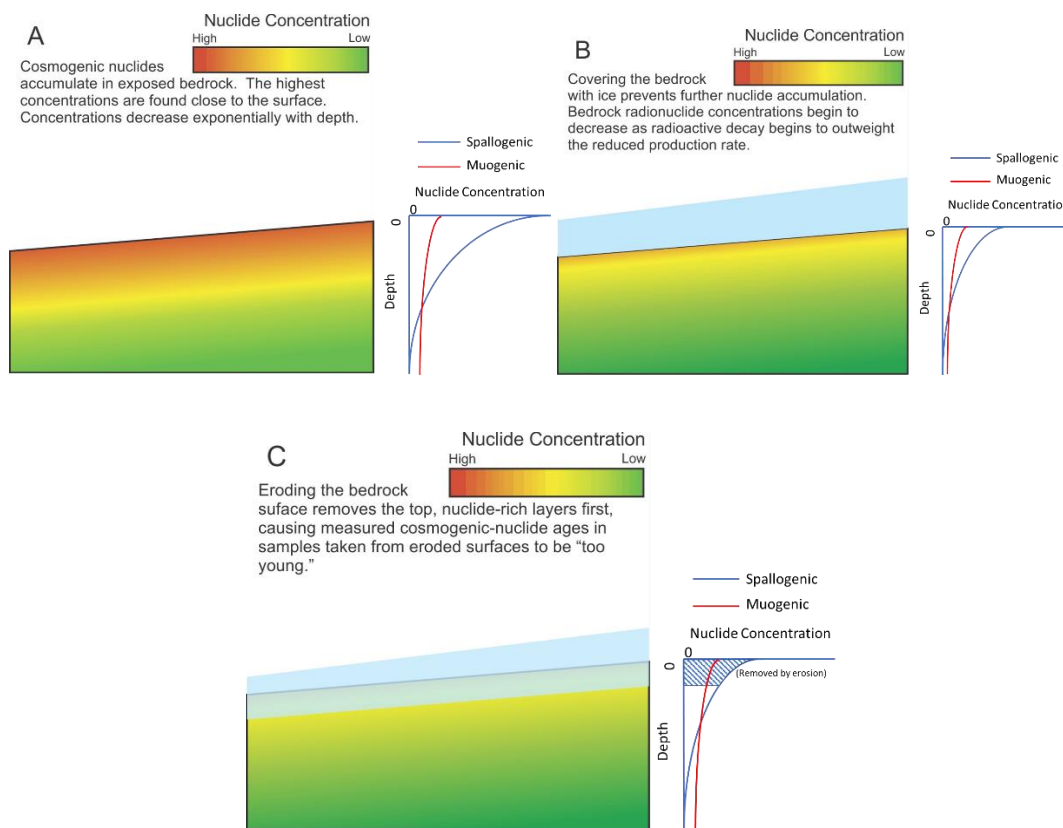


Figure 1.2. Schematic diagram demonstrating the accumulation, decay, and erosion of cosmogenic radionuclides. **A:** Cosmogenic nuclides accumulate in exposed bedrock. The highest concentrations are found close to the surface and concentrations decrease exponentially with depth. Muogenic production, while accounting for a smaller proportion of surface production, dominates production at depth as it is attenuated much less with depth. **B:** Covering the bedrock with ice (shown in blue) prevents further nuclide accumulation. The radionuclide concentration in the bedrock begins to decrease once radioactive decay outweighs the reduced production rate. **C:** Erosion of the bedrock surface removes the top, nuclide-rich layers first, causing measured cosmogenic-nuclide ages in a sample taken from an eroded surface to be “too young.”

rate depth dependence curves with nuclide concentrations in samples can constrain how long samples remained at certain depths below the surface.

When a sample is buried deeply enough by ice, snow, or sediment, production of new nuclides ceases but the radionuclides decay regardless. If the sample is uncovered again rapidly enough, some of the radionuclides may still remain in significant quantities. These “extra” nuclides will lead to an exposure age calculated solely from the nuclide concentration (an apparent exposure age) which overestimates the actual duration of the most recent period of exposure. On the other hand, a sample buried by moving glacial ice may be eroded away. When this happens, the uppermost, most nuclide-rich layers are preferentially removed, leading naïve exposure ages to underestimate the exposure duration of the sample (Fig. 1.2C).

The technique for detecting possible inheritance (“excess” nuclides accumulated during previous periods of exposure) in a sample relies on the fact that radionuclides inventories will decay while a sample is shielded from cosmic rays. Radionuclides with different half-lives will decay simultaneously but at different rates in an exposed sample. Once buried, however, the shorter-lived nuclide will decay more rapidly than will the longer-lived one, which causes the nuclide concentration ratio in the sample to evolve to favor the longer-lived nuclide. This evolution proceeds further as the burial duration increases. In the case of our samples, the radionuclides most useful for this application are ^{10}Be (half-life: 1.4 Myr) and ^{14}C (half-life: 5.7 kyr). Since the half-life of ^{10}Be is so much longer than that of ^{14}C , ^{10}Be can be treated as a stable isotope for the purpose of identifying burial episodes on ^{14}C timescales (~30 ka). Care must still be taken to not always accept these interpretations on face value, however, since ^{10}Be and ^{14}C are

produced via pathways with different attenuation lengths. The production rate of each nuclide, therefore, is dependent on the depth at which the nuclide is being produced, thus the production rate ratio of the two nuclides also varies with depth. If a sample has been eroded, the degree to which the ratio of the concentrations of the nuclides deviates from the actual production rate ratio may differ from its apparent value. I will elaborate on this phenomenon and how it relates to the observations made at Engabreen in Chapter 2.

1.4 Hypotheses

We hypothesize that our study site in the Engabreen forefield was exposed (not covered by glacial ice) for more than half of the Holocene, possibly in multiple episodes of exposure and that we will be able to test this hypothesis by examining cosmogenic radionuclide concentrations. The Holocene is generally considered a period of relative warmth after the Pleistocene ice age, although glaciers, particularly coastal glaciers, respond rapidly to even small fluctuations in climate. Determining the total exposure duration of the Engabreen forefield over the Holocene will reveal whether the retracted state of Engabreen approximates average glacial conditions over the Holocene or whether episodes of advance were temporally significant. We also hypothesize that lateral variations in nuclide concentrations across our study site will correspond to variations in basal sliding rates across Engabreen as per Hallet (1979), as loss of nuclides beyond that due to easily-modeled radioactive decay can be attributed to erosion. If this erosion is dominated by abrasion rather than plucking, the process will be heavily dependent on basal sliding velocity. The majority of this work will focus on the erosional aspect of these questions, specifically what in situ cosmogenic radionuclide concentrations can

reveal about the erosional processes that occurred at the bed of Engabreen during periods of ice cover.

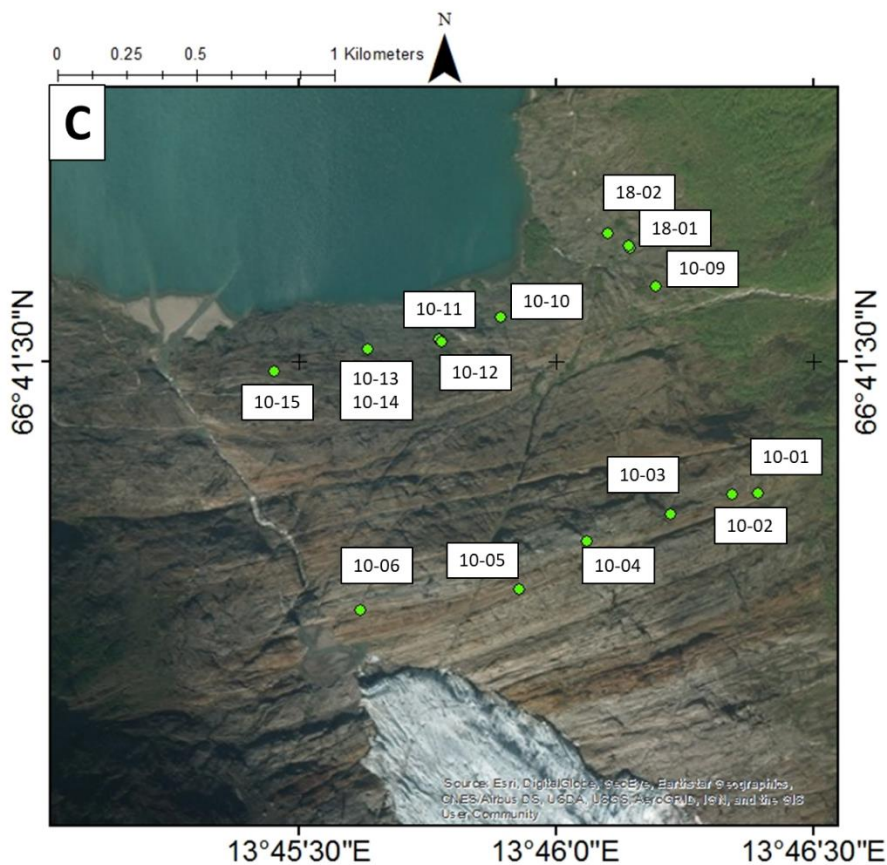
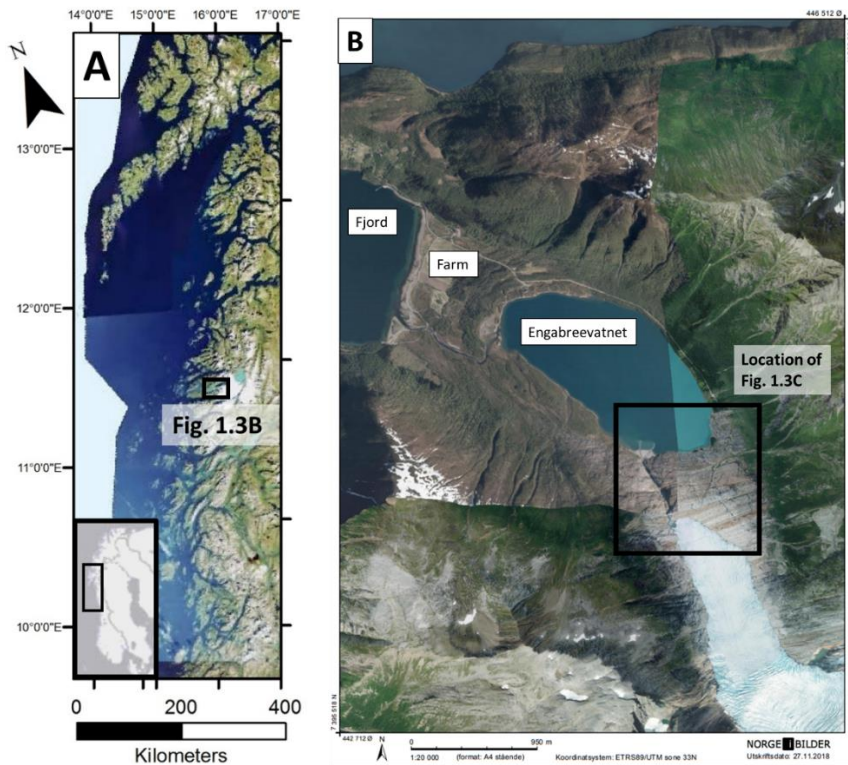
The remainder of chapter 1 provides background information about our methods and aims and describes the study location. Chapter 2 is written in the form of a manuscript to be submitted to a special issue on glacial erosion and sedimentation in *Annals of Glaciology*.

1.5 Setting

1.5.1 Location

Engabreen is an outlet glacier of the Svartisen Ice Cap of coastal northern Norway. Engabreen makes an attractive site for our study due to how well-studied the glacier is and its high latitude, low elevation location, which makes it very sensitive to changes in climate. The glacier is located at 66.6° N, 13.7° E and terminates ~ 200 m a.s.l. after descending ~ 0.5 km from the ice cap (Fig 1.3). Engabreen is the most heavily

Figure 1.3 (next page). Maps displaying the location of our study site on regional to local scales. Orthophotographs and maps in parts A and B courtesy of © Kartverket. **A:** Map showing the part of coastal Norway in which Engabreen is located. The black box marks the location shown in the orthophoto in Fig. 1.3B. An inset map (courtesy of Esri) in the lower right shows the location of this figure within the broader Scandinavian region. **B:** Orthophotos of the region surrounding our study site depicting Engabreen, an outlet glacier of Svartisen; Engabreevatnet, the proglacial lake; and Holandsfjorden to the North. The approximate location of a farm overrun by a glacier advance ca. 1723 CE (Karlén, 1988). The dominant foliation direction of the rock of the forefield is visible at this scale as color banding. The linear changes in color of both the lake and the surrounding land surface is an artefact of orthophotographs taken at different times, not an actual feature of the area. The black box marks the location shown in the Fig. 1.3C. **C:** Satellite photo of the Engabreen forefield, which contains our study site (image courtesy of Esri). Sample sites are marked with green circles and labeled with corresponding sample numbers. Slope-perpendicular Nye channels appear above and to the right of the glacier in the image as dark, linear features. The main outlet channel draining Engabreen is visible as a light linear feature extending from the toe of the glacier to the upper left corner of the image.



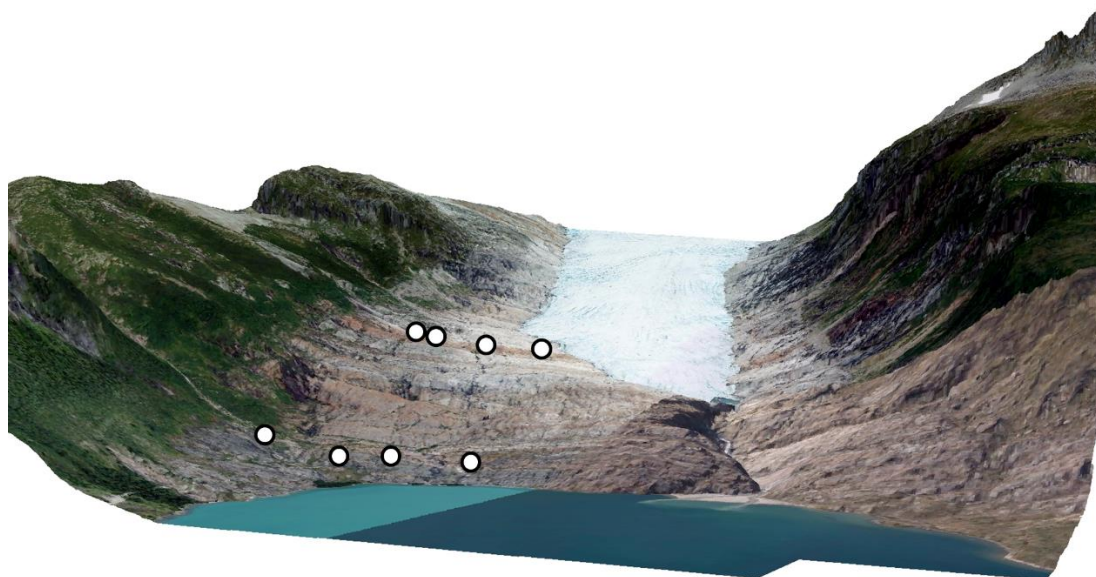


Figure 1.4. Up-valley view of our study site in the forefield of Engabreen consisting of orthophotographs draped over a digital terrain model. The glacier terminus can be seen near the center of the frame. Sample sites from which data was used in this study (white circles) are shown. Samples EG10-01 – 04 are our upper transect while samples EG10-09 – 14 are our lower one. The main Nye channel draining Engabreen can be seen at left on its way to Engabrevatnet at the lower end of the figure. The dominant foliation direction is East-West. The foliation is clearly visible in the color banding even at large scale, representing changes in the dominant mineralogy of the schists and gneisses of the forefield. The linear change in color of both the lake and the lower forefield is a consequence of orthophotographs taken at different times, not an actual feature of the area. Orthophotographs courtesy of © Kartverket.

instrumented glacier in Norway and has been monitored at times from both above and below the surface of the ice (e.g., Kennett *et al.*, 1993; Cohen *et al.*, 2000; Jackson *et al.*, 2005; Lappégard and Kohler, 2005; Iverson *et al.*, 2007). A tunnel dug beneath the glacier originally to divert meltwater for hydroelectric power generation is opened to the scientific community at times to allow for instrumentation, sampling, and direct observation of the basal layers of the glacier, its bed, and the ice-bed interface.

The glacial forefield stretches ~900 m between the trimlines (the lines separating fresh, eroded bedrock from the weathered, exposed bedrock) on the valley walls.

Topographically, it forms an asymmetric “W” shape near the lakeshore, with ~55m of relief in the middle, sloping outwards towards the valley walls, while up-valley it more resembles an asymmetric “V” (Fig 1.4). Low points in the valley are near its edges, where meltwater flowing into the valley collects into streams on its way to Engebrevatnet. The largest of these streams, near the left lateral margin of the valley, has carved a deep, narrow channel through which much of the meltwater emerging from beneath the glacier flows. This channel likely follows the path of the largest Nye channel formed underneath the glacier during a period of more extensive ice cover (Messerli, 2015). The ridges on the north and south walls of the valley rise to ~800 m a.s.l. and 320 m a.s.l., respectively. Our study utilizes samples collected from an area within the glacial forefield of Engabreen (30-140 m a.s.l. [Fig. 1.3C]).

The position of the terminus of Engabreen is well documented within historic times. Records of ice extent date to 1723 CE, when a homestead in the valley below Engabreen was overrun by ice (Karlén, 1988). When J. Rekstad surveyed Svartisen in the summers of 1890 and 1891, he reported that Engabreen terminated only 800 m from the beach, several km further downvalley from its current terminus (Rekstad, 1893). Locals at the time also told him that, 90 years prior to his visit (~1800 CE), Engabreen terminated into the waters of Holandsfjorden. Historical imagery confirms that the glacier extended into Engabreevatnet in the late 1800s (Fig 1.5). While the modern ice front is ~500m away from the study area, records indicate the site was covered until the late 1940s (Theakstone, 1965).

1.5.2 Climate

The Holocene climate of the North Atlantic was characterized by rapid shifts from colder to warmer conditions and vice-versa despite relatively stable, high-insolation orbital conditions (Bond, 1997). An overall trend of increasing temperatures contributed to the melting of the Laurentide and Scandinavian ice sheets at the end of the Pleistocene and continued into the Holocene, possibly driving these abrupt climatic fluctuations (Nesje *et al.*, 2004). Coastal Norway is a useful region for the study of this climatic period due to its location near the intersection of the Atlantic and Arctic oceans, with numerous maritime glaciers terminating near sea level or in deep fjords (Karlén and Kuylénstierna, 1996).

Outlet glaciers of the Scandinavian ice sheet retreated substantially during the early Holocene, although several short-lived readvances are preserved in continental and northern Atlantic records. Many of these glaciers appear to have melted away during the mid-Holocene as the climate warmed, although the timing of the retreat of glaciers in coastal, particularly northern, Norway is asynchronous (Nesje *et al.*, 2008).

Figure 1.6 shows LiDAR data revealing some of the important geomorphic features of the area. Moraines preserved at nearby Fonndalen (Fig. 1.6A), date to $12,000 \pm 200$ cal. years BP (Olsen, 2002) and indicates an ice front position near the current

Figure 1.5 (next page). Top: This 1889 image shows Engabreen was far more expansive in the nineteenth century than it is today. The terminus of the glacier is off the right edge of the image. Picture by Axel Lindahl (1889), https://blog.artfido.com/list_item/engabreen-glacier-norway-1889-2010/. **Bottom:** The glacier has retreated dramatically since the 1889 photograph was taken – the terminus has risen to ~200 m a.s.l., exposing a great deal of bare, formerly-subglacial rock. Picture by Dr. Brent M. Goehring (2010).



shoreline of Holandsfjorden at the end of the Pleistocene. Our study site is situated ~2 km from a series of moraines preserved near the mouth of the valley (Fig. 1.6B). The most distal of these (M.R.1 and M.R.2) are associated with a glacial advance around ~1200 C.E. (Worsley and Alexander, 1976). The more proximal moraines, therefore, may be associated with LIA advances centered around the 17th century (Winkler, 2003).

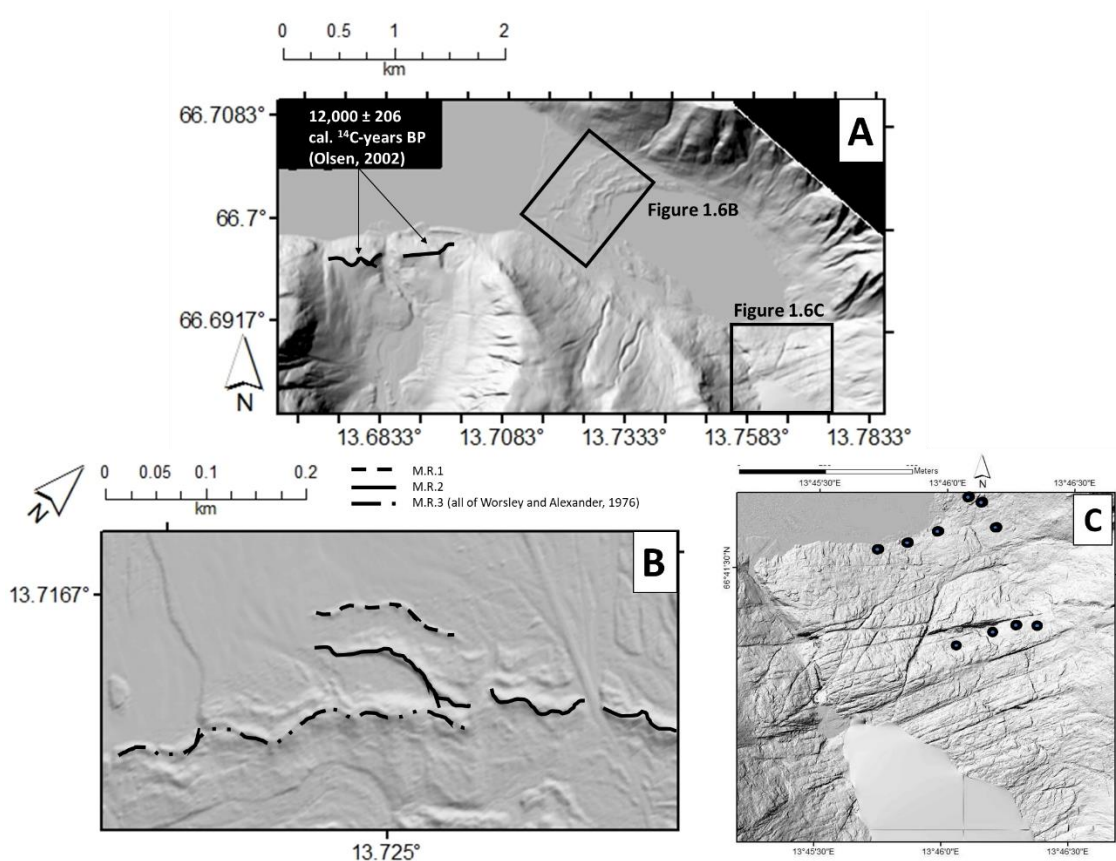


Figure 1.6. **A:** LiDAR data showing the valley into which Engabreen flows (right) and neighboring Fonndalen (left). Black lines mark moraines in Fonndalen dated to $12,000 \pm 60$ cal. years BP by Olsen (2002). We use this date to constrain the t_0 (initial exposure age) of Engabreen. Black boxes indicate the locations shown in Figs. 1.6B and 1.6C. **B:** LiDAR data showing the moraines exposed between Engabreevatnet and Holandsfjorden. Black lines mark moraines identified in Worsley and Alexander (1976), which are tentatively dated to ca. 1800 CE (Winkler, 2003). **C:** LiDAR data showing the Engabreen forefield. Sample sites are marked with circles.

**Chapter 2: The Distribution and Magnitude of Erosion Over Millennial Timescales
at Engabreen, Norway**

**The Distribution and Magnitude of Erosion on Millennial Timescales at Engabreen,
Norway**

Cari Rand¹, Dr. Brent M. Goehring²

¹Department of Earth and Environmental Sciences, Tulane University

²Department of Earth and Environmental Sciences, Tulane University

Corresponding Author:

Cari Rand

101 Blessey Hall,

New Orleans, LA

70118

E-mail: crand1@tulane.edu

Abstract

We present estimates of Holocene glacial cover and subglacial erosion rates from Engabreen, a temperate glacier in coastal northern Norway, that indicate that the current forefield of the glacier was buried for a total of approximately 1,000 years during the Holocene. Erosion rates along two transects perpendicular to glacier flow are highly variable, ranging from 0.24 to 4.36 mm yr⁻¹. We derive these estimates from in situ cosmogenic nuclide inventories, specifically those of ¹⁴C and ¹⁰Be, in bedrock exposed recently by the retreating Engabreen. In situ cosmogenic nuclide concentrations show no dependence on distance down or across the valley, leading us to believe that decreased nuclide concentrations in rocks relative to others with a shared exposure history are indicative of spatially variable erosion.

Muons produce ¹⁴C at higher rates than ¹⁰Be and produce both nuclides at greater depths than do spallation reactions, so the ¹⁴C-¹⁰Be concentration ratio increases with depth. The production rates of these nuclides by muons are less than spallation production rates, however, so nuclide ratios generated by production at depth can be rapidly overprinted by surface production rates. The observation of ¹⁴C-¹⁰Be concentration ratios elevated above the production ratio in samples of abraded bedrock indicates that sampled sites were deeply quarried during recent cover and then rapidly abraded prior to glacial retreat. This study shows ways that physical and chemical aspects of glacial landforms can reveal not just the modes of subglacial erosion that created them but also the locations and relative timing of specific erosional events.

2.1 Introduction

We measured in situ cosmogenic ^{14}C and ^{10}Be concentrations in samples of striated, polished bedrock exposed in the forefield of Engabreen, a glacier in coastal northern Norway (Fig. 1.3). The relationship between these two concentrations allows us to estimate the net duration of ice cover at our site during the Holocene and average erosion rates over that duration. As we will show, the concentrations indicate a very short total burial duration with implications regarding the timing of erosion at the site. In particular, the concentration ratio in our samples indicates that plucking and abrasion took place recently.

Glaciers are sensitive to changes in climatic conditions and can respond to changes in temperature and precipitation rate over very short timescales (e.g., < 1 year; Oerlemans, 2005). Since advancing glaciers often destroy records they created during more contracted periods, geomorphic evidence (e.g., moraines, striae) predominantly record episodes of extended glacial cover (Benn and Evans, 2014). Our ability to constrain the past length of glaciers therefore relies on observable evidence which is not destroyed by glacier readvances. In situ cosmogenic nuclide concentrations increase during exposure and decrease during burial and erosion. Calculating the rates at which these concentrations change allows us to determine the integrated duration for which a given pro-glacial bedrock surface was covered by ice since the surface was last reset by a lengthy period of burial.

Samples of actively-eroding subglacial bedrock are difficult to collect due to the challenges involved in accessing the beds of glaciers. Determining the rate at which bedrock is removed by erosion can be arduous and often relies upon proxy data rather

than direct measurement. Boreholes and slab experiments (e.g. Lappégard and Kohler, 2005; Iverson *et al.*, 2007) allow direct measurement of erosion rates but can only provide data over short timescales (on the order of years) and must be repeated at numerous locations under a glacier to reveal spatial patterns of erosion. Techniques that examine glacial sediment volumes allow one to estimate erosion over much longer timescales but are less precise and are heavily dependent on subglacial and proglacial hydrology (e.g., Riihimaki *et al.*, 2005); this hinders the study of the evolution of glacial landscapes. When incorporating data long and short duration studies into models of glacial landscape evolution, one must therefore be careful that one's results can be accurately scaled to the timeframe one examines. Better constraints on the magnitude of subglacial erosion would aid in modeling the history of glacial and post-glacial areas and better understanding the spatial distribution of erosion underneath glaciers would improve interpretations of the forms created by glacial erosion.

Our technique for estimating glacial erosion rates using in situ cosmogenic nuclide concentrations occupies the middle ground between these other techniques. Measurements can be made at multiple locations with relative ease as samples can be taken from exposed bedrock, and the data gathered reveals erosion rates over millennial timescales, bridging the gap between the short- and long-term scales examined by other methods and improving spatial resolution and coverage by allowing us to target specific glacial features.

2.2 Background

Cosmogenic nuclides such as ^{14}C and ^{10}Be are created by the interactions between cosmic rays and matter near the surface of the Earth. These cosmic rays are attenuated

by the matter through which they pass, meaning that interactions become less and less frequent as one descends below the surface. Different types of production pathway have different attenuation lengths. The most productive production pathway, spallation, is rapidly attenuated and thus rarely produces nuclides below ~5 m of bedrock. Other production pathways such as muons produce nuclides at a lower rate than does spallation but are much less rapidly attenuated. Production at depths from ~5-100 m, therefore, is dominantly by muons (e.g.; Farber *et al.*, 2008; Briner *et al.*, 2016).

The concentration of cosmogenic nuclides in a sample increases with the duration and degree of its exposure until a sample reaches secular equilibrium, the state in which production of nuclides is balanced by loss to radioactive decay. In its simplest case, the exposure age of a sample can be calculated from the concentration of a given nuclide. This calculation is complicated, however, by processes such as radioactive decay and erosion because they remove accumulated nuclides. Additionally, short episodes of burial may only partially deplete nuclide concentrations, leaving a rock with “inheritance” (nuclides produced during multiple episodes of exposure). Different nuclide species are produced in rock at different rates and different radionuclide species decay at different rates. Events in the history of a sample alter the concentrations and ratios of nuclides in a potential sample in characteristic ways. Halting nuclide production in a sample (e.g., by burying it) will modify nuclide ratios in favor of the longer-lived nuclide since that nuclide will decay at a slower rate. Removing nuclides through erosion will also alter these ratios, but in favor of the less depth-dependent nuclide. Analyzing multiple cosmogenic nuclides potentially allows one to identify and resolve events and processes which affected a sample in the past.

^{10}Be is a frequently-used nuclide for exposure dating because its half-life (1.394 Myr) sets its effective usable range from centuries to millions of years, respectively (Nishiizumi *et al.*, 2007). ^{14}C , owing to its much shorter half-life (5.7 kyr), is a useful nuclide to pair with ^{10}Be to identify burial episodes and erosion on Holocene timescales. The production rates of ^{14}C and ^{10}Be are also dependent on depth to different degrees, which aids in estimation of the timing of plucking events. The nuclide ratio in a sample at depth, exposed by a plucking event, will be rapidly overprinted by production at the surficial rate. In a sample with a history characterized by exposure, then, a surviving nuclide ratio indicative of production at depth implies that the plucking event which exposed it must have been recent and any overprinted abrasion rapid and subsequent.

2.3 Setting

Engabreen is an outlet glacier of Svartisen ice cap in coastal Norway (Fig. 1.3). Terminal moraines at nearby Fonndalen date to $12,000 \pm 200$ ^{14}C -years BP (Olsen, 2002), indicating that glaciers terminated near the current fjord shore at the end of the Older Dryas (ca. 14 ka). Moraines between the current terminus of Engabreen and Holandsfjorden are tentatively dated to ca. 1200 CE (Worsley and Alexander, 1976) and historical records of ice advance (Fig. 1.5, Karlén, 1988) show that the Engabreen terminus was several kilometers longer and terminated near sea level in historic times. The terminus has since retreated to ~200 m a.s.l., exposing a bedrock forefield consisting dominantly of amphibolite and biotite garnet schists (Sigmond *et al.*, 1984). The dominant bedrock foliation strikes perpendicular to sub-perpendicular to the ice flow. In general, the bedrock surface is polished and striated, and many areas display crescentic gouges and plucking (see Appendix A). The forefield has a stepped habit descending as a

series of rounded ridges or benches separated by a multitude of channels ranging from a few centimeters to several meters deep.

2.4 Methods

2.4.1 Sampling Methods

We sampled along two transects – one ~200 m from the Engabreen terminus at ~150 m a.s.l. and the other ~500 m from the terminus at ~20-30 m a.s.l. Samples were collected with a hammer and chisel. Topographic shielding was measured at each sample site by measuring the azimuth and inclination of horizon obstructions in a full circle around each sample. Topographic shielding corrections as well as sample location and size data are presented in Table 2.1. Our results are based on several assumptions: that glacial cover/erosion during the Last Glacial Maximum was sufficient to decrease cosmogenic ^{10}Be and ^{14}C concentrations in the bedrock of our study site below detection limits, that snow cover at our sites was transient (Theakstone, 2013), and that snow cover and any subaerial erosion were negligible over the timescales in question. Due to the maritime climate at Engabreen, temperatures regularly rise above freezing even during the winter months and the ground is commonly free of snow by mid-spring (Andreassen *et al.*, 2006).

The transects from which we sampled generally span the forefield from the right lateral valley wall to near the middle of the valley. We assume that samples from a given transect have the same exposure history because the transects extend perpendicularly to ice flow.

Our sampling strategy, which targeted sites atop bedrock ridges and rises, lends us confidence that no substantial erosion of the sample surfaces was carried out by streams, which preferentially flow through depressed channels along foliation planes and through former Nye channels at this site (Messerli, 2015). This strategy additionally minimizes the effect of transient till cover at our sites, further reducing the complexity of interpreting our results. We scaled sea level, high latitude production rates from the calibration dataset of Stroeve *et al.* (2015) to our sample sites using the scaling scheme of Stone (2000). Due to the high latitude, low elevation location of our samples, this scaling scheme is appropriate. Different scaling schemes, however, do not significantly alter our results.

Striation and foliation orientation data were collected using the edge of a tablet computer equipped with a magnetometer, accelerometer, and gyroscope to simulate a compass and inclinometer and recorded on the FieldMove digital mapping application.

Samples were crushed, quartz fractions isolated, and divided into aliquots for ^{10}Be and ^{14}C analysis. Aliquots for ^{10}Be analysis were dissolved in concentrated HF, ~ 0.25 g ^9Be carrier added, and Be isolated from other ions by ion exchange column chemistry and precipitated at the Tulane University Cosmogenic Nuclide Laboratory (TUCNL) following standard laboratory procedures. $^{10}\text{Be}/^9\text{Be}$ ratios were determined via accelerator mass spectrometric (AMS) analysis at the Purdue Rare Isotope Measurement Lab. ^{14}C extraction was carried out at TUCNL following methods outlined in Goehring *et al.* (2019) and $^{14}\text{C}/^{13}\text{C}$ ratios measured at the National Ocean Science Accelerator Mass Spectrometry facility. Stable C isotopes were measured at the University of California, Davis Stable Isotope Facility. Data reduction followed Hippe and Lifton (2014).

2.4.2 *Mathematical Methods*

2.4.2.1 *Data Reduction*

Reported isotope ratios for Be and C were converted to concentrations (N, atoms g⁻¹) via the following equation:

$$N = \frac{(R*S)-B}{M} \quad (2.1)$$

in which R refers to the measured nuclide ratio reported by the AMS laboratory (¹⁰Be-⁹Be and ¹⁴C-¹²C, respectively), S the atoms of carrier (which contains both the added carrier and sample atoms), B the atoms in the blank (which contains only the added carrier), and M the mass of the sample.

This method relies upon the assumption that effectively all of the beryllium-9 (⁹Be) in the sample is contributed by the added carrier. We consider this a reasonable assumption for our location as the rocks we sampled bore neither beryl, other notable Be-bearing minerals, nor alteration products of such. We have confidence in a similar assumption, that all of the ¹⁴C in the sample was produced in situ, because our method involved etching the surface of the sample quartz and then baking it at high temperatures for several hours to remove meteoric contamination.

2.4.2.2 *Isochron Method*

An isochron plot (Fig. 2.1) is a graph with the concentrations of two nuclides, at least one of which decays radioactively, plotted along its axes. The accumulation of a radionuclide in surface rocks on this kind of plot is given by the following equation:

$$N = \frac{P(0)}{\lambda + \frac{\varepsilon}{\Lambda}} (1 - e^{-\lambda t_e}) e^{-\lambda t_b} + \frac{P(z_b)}{\lambda} (1 - e^{-\lambda t_b}), \quad (2.2)$$

in which N is the concentration of the nuclide in question (atoms g^{-1}), $P(0)$ its production rate at the surface, λ its decay constant ($4.998\text{e-}7 \text{ yr}^{-1}$ for ^{10}Be , $1.216\text{e-}4$ for ^{14}C), ε the erosion rate, Λ the attenuation length of the production pathway of interest (we use 160 g cm^{-2} for spallation), t_e and t_b the respective exposure and burial durations of the sample, and $P(z_b)$ the production rate of the nuclide at depth z_b . The first term of this equation describes the accumulation of nuclides during periods of exposure and the second the accumulation of nuclides at a reduced rate during periods of burial. We assume, however, that Engabreen buried our samples deeply enough to reduce the second term of this equation to near zero. Samples will thus plot further and further from the origin of the graph as they accumulate nuclides (i.e., as their exposure durations increase). Due to the difference in half-life of the two nuclides in question, samples which have been buried for the same length of time will all plot along a ray drawn from the origin of the graph. The slope of the ray fit to unburied samples will equal the ratio of the production rates of the measured nuclei and, as the burial duration increases, this slope will change such that the ray is “rotated towards” the axis on which the longer-lived nuclide is plotted. Dating approaches that use multiple nuclides, such as the one we use here

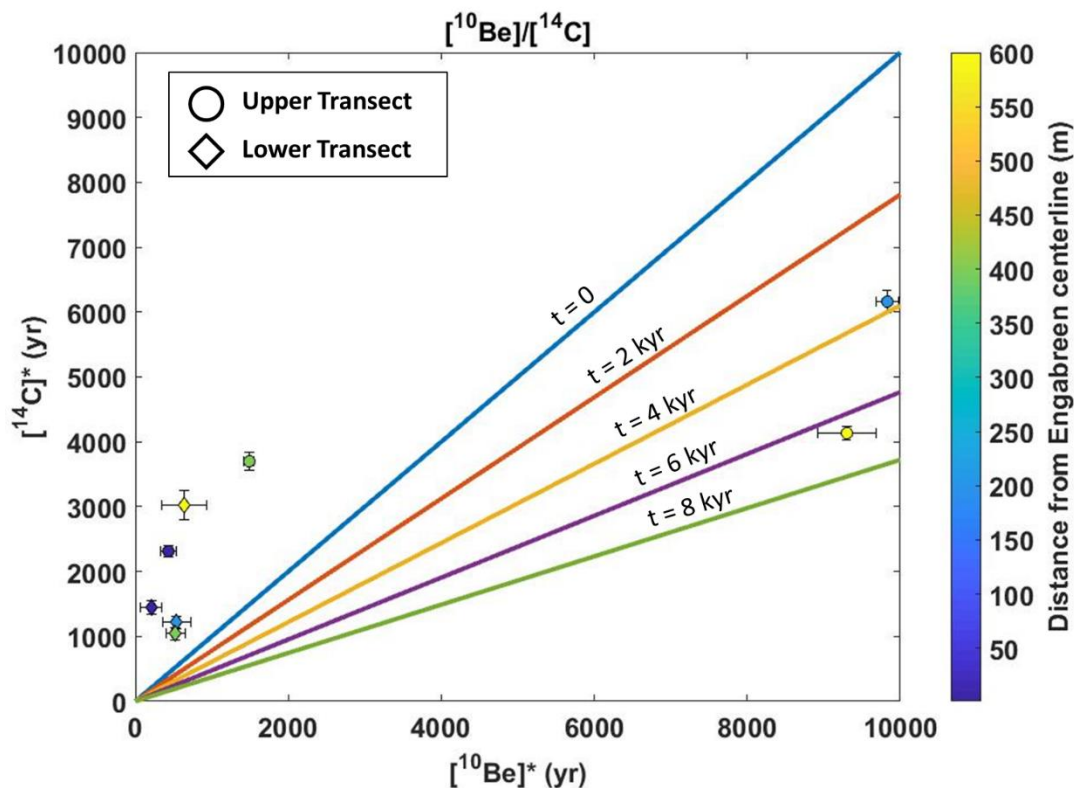


Figure 2.1. Isochron diagram demonstrating the behavior of a two-radionuclide (^{10}Be and ^{14}C) system over time. Nuclide concentrations of the two nuclides are plotted on the axes. Note that each concentration is normalized by dividing by the production rate of that nuclide, thus the unit of these values is actually years. Samples with similar burial durations will plot along an isochron, depicted above as colored lines. Isochron labels here indicate the burial duration of samples plotting along each respective isochron. Unburied samples will plot along the line labeled “ $t=0$ ”, the slope of which is identical to the production rate ratio of the nuclide plotted on the y-axis to that of the nuclide plotted on the x-axis. As the burial duration increases, the slope of the corresponding isochron approaches that of the axis on which the longer-lived nuclide is plotted (the x-axis in this figure). The distance from the origin along an isochron at which a sample plots increases with increasing pre-burial exposure time and decreases as a sample surface is eroded. It is important to note that these isochrons are calculated using surface production rates and are thus approximations. Substantial erosion will expose samples which accumulated nuclides at different rates, which is why samples can plot above the $t=0$ isochron. Samples with little to no exposure and heavily eroded (depleted) samples will therefore plot near the origin of the graph. The upper transect samples with high concentrations have concentrations consistent with 2-8 kyr of cover while the lower samples and the upper samples with low concentrations plot above the $t=0$ isochron, indicating enhanced ^{14}C production relative to ^{10}Be . Note, however, that this plot does not take erosion into account. We assume that each sample in a given transect has a similar exposure history, so variations in nuclide concentration are actually indicative of variable erosion rates across a transect.

(developed in Goehring [2013]) allow us to graphically interpret the data from our sample transects. Samples from one transect should all have the same exposure and burial history.

Using the methods detailed in Goehring *et al.* (2013), we used a Bayesian isochron fitting method to calculate the probability density function (PDF) for the exposure duration (t_e) of each transect. This method allows us to calculate the β value of our samples, a parameter which describes the depth dependence of ^{14}C production relative to that of ^{10}Be production in the bedrock. This relative depth dependence depends on the proportion of nuclides of each species produced by different production pathways and is location dependent. ^{14}C has a greater muogenic production than does ^{10}Be , which informs where we expect to find high β values (Heisinger *et al.*, 2002a, 2002b). At low latitudes, the inclination of the magnetic field of the Earth is more horizontal and, thus, unfavorable for allowing charged particles to pass through it. This phenomenon results in a higher cutoff rigidity at lower latitudes, meaning that a given particle requires a higher level of momentum in order to pierce the magnetic field of the Earth without being deflected away from the surface at these latitudes (Gosse and Phillips, 2001). Spallation reactions are significantly mediated in their intermediate stages by neutrons (see Fig. 1 of Gosse and Phillips, 2001). Fluxes of neutrons, particularly low-energy neutrons created by spallation reactions are therefore proportionally greater at lower latitudes compared to fluxes of charged, but weakly interacting, particles such as muons (Farber *et al.*, 2008). Neutrons additionally have shorter attenuation lengths than do muons, meaning that neutron fluxes will be proportionally greater at higher elevations where the atmosphere is thinner (Briner *et al.*, 2016). Taken together, this contributes to two trends we anticipate

in β values. We can expect to see greater β values, indicating proportionally lesser muon fluxes, at (1) low latitudes and (2) high elevations, or a combination of the two. This means that, at higher latitudes and/or lower elevations, ^{10}Be production will drop off more quickly with depth than will ^{14}C production.

2.4.2.3 Erosion Rate Calculations

We used the method of Goehring *et al.* (2013) to identify the average values of t_e and β , the two variables in which we are interested. Subtracting t_e from t_0 allows us to determine the integrated burial duration of the transect. Given our measured in situ ^{14}C and ^{10}Be concentrations; β , representative of the relationship between ^{10}Be and ^{14}C production at a given depth; and t_e , from which surface nuclide concentrations can be predicted, we numerically identified the depth to which each sample has been eroded.

We modeled the attenuation of ^{10}Be production with depth via the following equation:

$$P_{10}(z) = P_{10}(0)\varphi(z) \quad (2.3)$$

in which $P_{10}(z)$ is the ^{10}Be production rate at depth z ($z = 0$ denotes the surface) and φ a term denoting the depth dependence of ^{10}Be production. $\varphi(z)$ typically takes the form of a negative exponential as production decreases with increasing mass depth. The production rate of ^{14}C is related to the ^{10}Be production rate at a given depth by

$$P_{14}(z) = P_{14}(0) * (\beta\varphi(z) + 1 - \beta) \quad (2.4)$$

in which $P_{14}(z)$ is the ^{14}C production rate at depth z and $P_{14}(0)$ is the ^{14}C surface production rate. Where $\beta < 1$, the ^{14}C production rate is less attenuated than that of ^{10}Be .

The equations describing measured nuclide concentrations in a given sample i are then considered in the following two equations:

$$N_{10i} = P_{10i}\varphi(z_i)t_e \quad (2.5)$$

$$N_{14i} = \frac{P_{14i}}{\lambda_{14}} [\beta\varphi(z) + (1 - \beta)](1 - e^{-t_e\lambda_{14}})e^{-(T_0 - t_e)\lambda_{14}} \quad (2.6)$$

in which N_{10i} and N_{14i} (both atoms g^{-1}) and P_{10i} and P_{14i} (both atoms $g^{-1} yr^{-1}$) are the ^{10}Be and ^{14}C concentrations and scaled production rates at the surface in sample i , respectively. λ_{14} is the decay constant of ^{14}C and t_e the exposure duration of the sample.

Solving for $\varphi(z)$ in Eq. (3) allows us to substitute this value into Eq. (4) to generate the equation for an isochron:

$$\frac{N_{14i}}{P_{14i}} = \frac{1}{\lambda_{14}} \left[\beta \left(\frac{N_{10i}}{P_{10i}t_e} \right) + (1 - \beta) \right] (1 - e^{-t_e\lambda_{14}})e^{-(T_0 - t_e)\lambda_{14}} \quad (2.7)$$

which shows the ^{14}C concentration (normalized to its production rate) as a function of ^{10}Be concentration. Were the erosion rate already known, we could have simply divided the depth by the erosion rate to calculate the burial duration. Since we did not know the erosion rate at each sample site, however, we used the isochron method, in which the exposure duration of the transect is determined from the slope of the generated isochron. If every sample in a transect is assumed to have the same burial and exposure durations, then younger apparent exposure ages correspond to increased glacial erosion. The magnitude of this erosion can be calculated by solving for $\varphi(z)$ in Eq. 3, then solving for z numerically using the following equation:

$$\varphi(z) = P_{sp}e^{-\frac{z\rho}{\Lambda_{sp}}} + P_{\mu-}e^{-\frac{z\rho}{\Lambda_{\mu-}}} + P_{\mu f}e^{-\frac{z\rho}{\Lambda_{\mu f}}} \quad (2.8)$$

in which μ_{sp} indicates spallation and μ_{-} and μ_{f} indicate negative and fast muons, respectively (i.e. P_{10sp} would refer to the production rate of ^{10}Be via spallation, Λ_{μ_f} the attenuation length of production by fast muons, etc.). We determined 1σ error ranges on the erosion depths via 500-point Monte Carlo bootstrapping as per the method of Goehring *et al.* (2013). We then converted these erosion depths to erosion rates by dividing by the calculated exposure duration for the transect.

It is important to note, however, that inferences regarding the timing of any episode of burial must be drawn from other sources – the isochron method yields only integrated durations, which do not represent a unique solution to that problem. Outside information must be utilized to discern between one longer or multiple shorter episodes of burial as the isochron method only reveals the total burial duration since the sample concentrations were last reset. The radiocarbon ages of plant samples uncovered by melting glaciers are often used to constrain the past extents of the glaciers (e.g., Lowell *et al.*, 2013; Miller *et al.*, 2013). This sort of sample is hard to come by at Engabreen, however. The broad expanse of bare rock forming the floor of the valley seems to have been scoured quite clean by the glacier during its more extensive state and by frequent washing by meltwater and rain since. Inferences drawn from external paleoclimate records allow us to constrain the relative size (i.e., larger/smaller than at present) of the glacier in the past.

Table 2.1.

Sample locations and parameters

Sample	Transect	Latitude (° N)	Longitude (° E)	Elevation (m a.s.l.*)	Thickness (cm)	Topographic Shielding Correction
EG10-01	Upper	66.68997	13.77321	181	2.25	0.9554
EG10-02	Upper	66.68996	13.77235	168	1.43	0.9700
EG10-03	Upper	66.68966	13.77007	155	1.79	0.9700
EG10-04	Upper	66.68918	13.76658	146	2.00	0.9667
EG10-09	Lower	66.69263	13.76990	27	1.93	0.9474
EG10-10	Lower	66.69223	13.76488	20	3.21	0.9574
EG10-12	Lower	66.69195	13.76289	24	2.05	0.9855
EG10-13	Lower	66.69182	13.76057	32	2.52	0.9698
EG10-14	Lower	66.69182	13.76057	32	1.90	0.9615

2.5 Results

2.5.1 Cosmogenic Nuclide Concentrations

Each sample has ^{10}Be and ^{14}C concentrations above detection limits, indicating that the sample site has been exposed for sufficient time to generate an inventory and not eroded deeply enough to remove said inventory. The concentrations do not vary in a systematic way with distance along a transect perpendicular to the flow of Engabreen but concentrations in lower transect samples are lower by roughly an order of magnitude compared to concentrations in upper transect samples.

^{10}Be concentrations vary across the upper transect by an order of magnitude (Table 2.2), yielding apparent ^{10}Be exposure ages of 0.4-9.1 ka. The concentrations do not vary systematically with distance from the valley walls or relative elevation (Fig. 2.2). The samples with the highest concentrations (EG10-02 and EG10-04) are adjacent to the samples with the lowest concentrations (EG10-01 and EG10-03).

^{10}Be concentrations for the lower transect are much lower than the upper transect and yield naïve ^{10}Be exposure ages of 0.21-0.59 ka. Similarly to the upper transect, these concentrations do not vary systematically with their location in the valley other than that they are all substantially lower concentrations than the upper transect. Samples EG10-13 and EG10-14 are from the same location – EG10-14 was collected from a vertical lee face and EG10-13 from the stoss side of the same face. ^{14}C concentrations were not measured from sample EG10-14 because the sample only contained enough quartz for ^{10}Be analysis.

Table 2.2.

Cosmogenic nuclide concentrations and apparent exposure ages

Sample	Transect	[¹⁴C][†] (atoms g⁻¹)	±1σ (atoms g⁻¹)	¹⁴C age	±1σ (ka)	[¹⁰Be]^{††} (atoms g⁻¹)	±1σ (atoms g⁻¹)	¹⁰Be age	±1σ (ka)
EG10-01	Upper	4.16e+4	1.54e+3	2.658	0.245	2.10e+3	4.96e+2	0.411	0.199
EG10-02	Upper	11.1e+4	3.19e+3	11.310	1.519	45.4e+3	6.81e+2	9.082	0.870
EG10-03	Upper	6.56e+4	2.44e+3	4.896	0.544	7.11e+3	3.06e+2	1.384	0.185
EG10-04	Upper	7.11e+4	1.86e+3	5.526	0.455	44.2e+3	17.9e+2	9.046	1.173
EG10-09	Lower	2.26e+4	1.54e+3	1.513	0.230	0.876e+3	5.75e+2	0.208	0.275
EG10-10	Lower	1.87e+4	1.48e+3	1.248	0.216	2.20e+3	7.39e+2	0.500	0.341
EG10-12	Lower	1.63e+4	1.49e+3	1.060	0.208	2.18e+3	5.20e+2	0.489	0.240
EG10-13	Lower	4.80e+4	3.49e+3	3.666	0.682	2.70e+3	12.6e+2	0.586	0.550
EG10-14	Lower	-	-	-	-	0.936e+3	4.30e+2	0.220	0.203

All apparent exposure ages are calculated via the CRONUS-Earth online exposure age calculator (version 3) using production rates scaled to sea level high latitude using the Lifton-Sato-Dunai nuclide-specific scaling scheme (Hippe and Lifton, 2014) and corrected for topographic shielding.

[†]¹⁴C concentration

^{††}¹⁰Be concentration

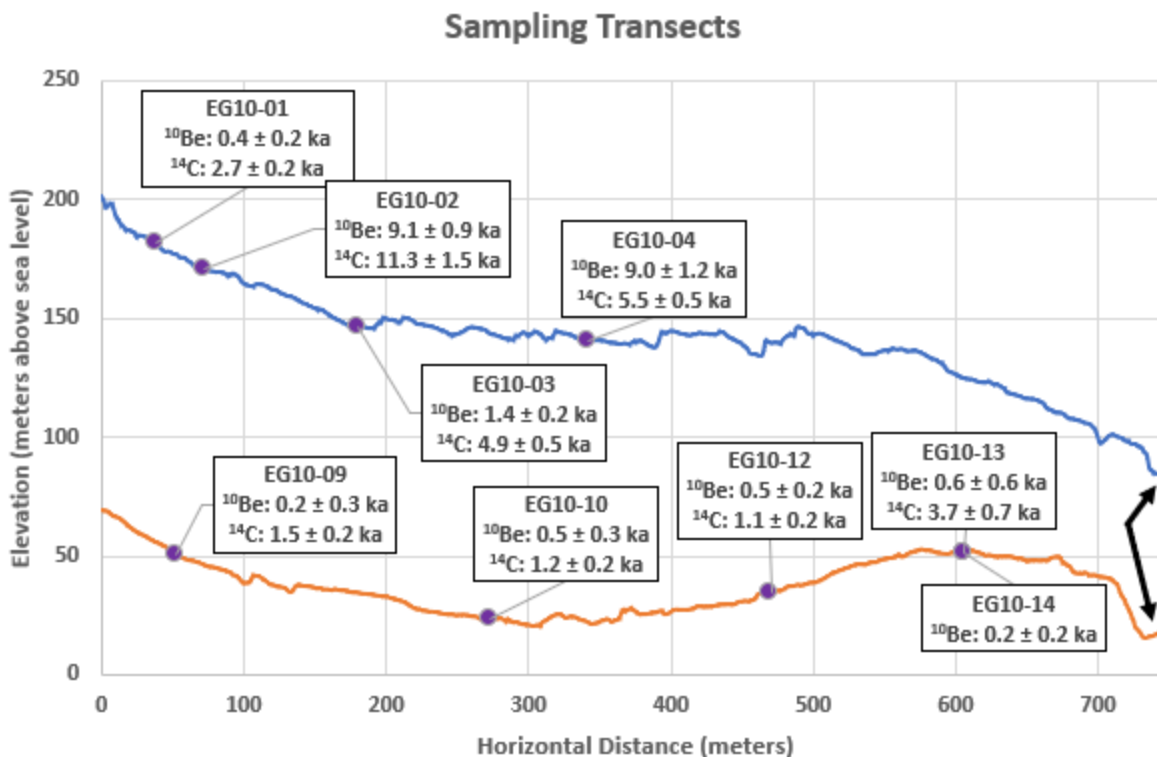


Figure 2.2. Elevation profiles of our two sampling transects. Sample sites (purple circles) are shown projected onto the upper (blue line) and lower (orange line) transects. The y-axis corresponds to the eastern valley wall (you are looking upvalley in this figure). Samples are labeled with their sample name and apparent ^{10}Be and ^{14}C ages where available. The main Nye channel carrying meltwater out from below Engabreen along the right-lateral wall of the valley is denoted with a black arrow. It is evident from this data that neither proximity to the valley wall nor elevation are the primary control on nuclide concentrations, which vary significantly even between nearby samples. Elevation data from the Norwegian Mapping Authority.

^{14}C concentrations also vary across both transects independently of position and relative elevation within a transect. The proportional decrease in concentrations from the upper transect to the lower, however, is less for ^{14}C than it is for ^{10}Be . Upper transect ^{14}C ages range from 2.667 to 11.217 ka and those from the lower transect between 1.038 and 3.703 ka.

2.5.2 Exposure History

We calculated an exposure duration for our study site of 11.0 ± 0.2 kyr using the methods outlined in section 2.4.2.2 (Fig. 2.3). Given the close spatial proximity of our two transects, we calculated the exposure duration using all of our samples instead of calculating separate exposure durations for each transect. Recent and historical rates of retreat (Fig. 1.5; Rekstad, 1893) indicate that Engabreen is capable of retreating the ~ 300 m between our two transects within the 200 yr of the 1σ uncertainty on our calculated exposure duration. Subtracting this duration from the initial exposure age of 12.0 ka assumed from Olsen (2002) gives a burial duration of 1.0 ± 0.2 kyr for the study site.

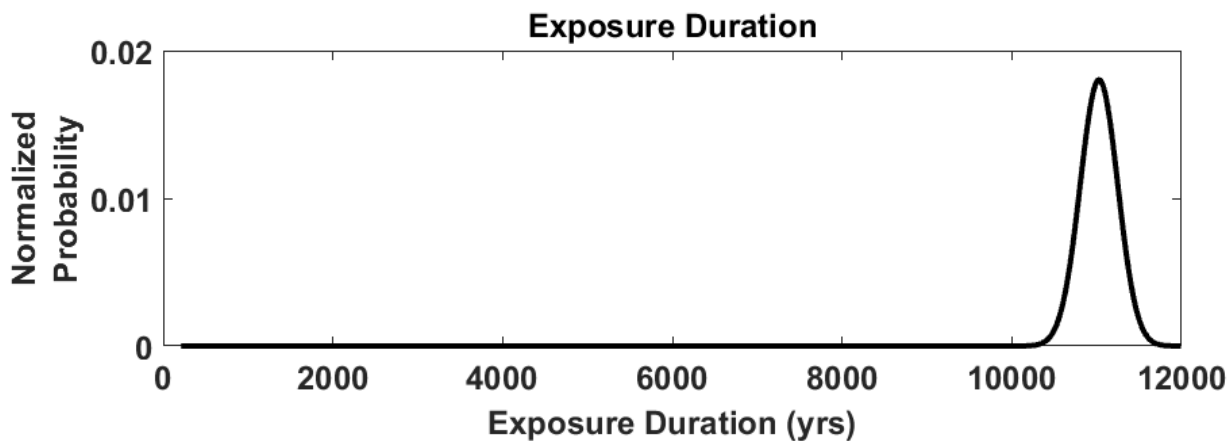


Figure 2.3. Probability density for exposure duration t_e for our transects. Note the relatively narrow, symmetric distribution of probable exposure durations centered around $t_e = 11,400$ yr. The close spatial proximity of our two transects (separated by ~ 300 m and ~ 125 m of elevation difference) indicates that the exposure histories of the two are likely extremely similar. This calculation assumes that the samples possessed no inherited ^{10}Be when exposed after the last glacial maximum

2.5.3 Erosion Depths

Calculated erosion depths, like the nuclide concentrations reported above, do not vary systematically with position in the forefield or relative to the glacier (Table 2.3). Erosion depths vary by more than an order of magnitude as well along the upper transect and to a lesser degree along the lower transect and sites with very different erosion depths are located adjacent to one another. Measurement uncertainty increases proportionally when the nuclide concentration in a sample is low, which is reflected in the flatter error distributions surrounding calculated erosion depths for our lower transect relative to those of our upper transect (Fig. 2.4).

Table 2.3.

Calculated erosion depths and rates and ^{14}C - ^{10}Be concentration ratios.

Sample	Transect	Erosion Depth (m)	Erosion Rate (mm yr ⁻¹)	[^{14}C]:[^{10}Be] [†]
EG10-01	Upper	2.15 ± 0.14	2.15 ± 0.14	19.8 ± 0.24
EG10-02	Upper	0.11 ± 0.01	0.11 ± 0.01	2.4 ± 0.03
EG10-03	Upper	1.25 ± 0.02	1.25 ± 0.02	9.2 ± 0.06
EG10-04	Upper	0.11 ± 0.02	0.11 ± 0.02	1.6 ± 0.05
EG10-09	Lower	2.39 ± 0.53	2.39 ± 0.53	25.8 ± 0.66
EG10-10	Lower	1.62 ± 0.28	1.62 ± 0.28	8.5 ± 0.34
EG10-12	Lower	1.64 ± 0.27	1.64 ± 0.27	7.5 ± 0.26
EG10-13	Lower	1.50 ± 0.20	1.50 ± 0.20	17.8 ± 0.47

Erosion depths calculated using the integrated exposure duration determined using the Bayesian isochron method (see Appendix C). Burial durations determined by subtracting the integrated exposure duration from the initial exposure age. Erosion rates calculated by dividing the erosion depth by the burial duration. ^{14}C was not measured from sample EG10-14, so it was omitted from these calculations.

[†] ^{14}C - ^{10}Be concentration ratio

Figure 2.5 shows the joint t_e and β probability density function as a contour plot using the T_0 of 12 ka of Olsen (2002). From it, one can see that the most likely exposure duration and β value of the upper transect are greater than those of the lower transect. Additionally, one can see the wider distributions of possible values for both parameters for the lower transect compared to the upper.

2.5.4 *Glacial Striae*

We collected striation and foliation data from the transects at our study site (Fig. 2.6). The results show striation trends broadly dominated by the ice flow direction to the north-northwest, but trends differ slightly between transects. The lower transect contains a slightly more prominent eastward component of ice flow, especially on the eastern edge of the transect, than does the upper transect, which is closer to the current terminus. Foliation strike is dominated by an east-west trend at both transects resembling the trend of large scale undulation of the bed between flow-perpendicular Nye channels.

2.6 Discussion

2.6.1 *Cosmogenic Nuclide Concentrations*

We assume that our sample sites contained no inherited nuclides at the end of the last glacial maximum and thus that current cosmogenic nuclide inventories represent solely Holocene exposure. The stark differences in nuclide concentrations between samples with similar exposure histories and lack of spatial trend is unintuitive, therefore. The greatest proportional variation is visible in ^{10}Be concentrations, and we discuss the source of this variation here. The sharpest spatial variation is between samples EG10-13 and EG10-14 (Table 2.2, Figure 2.2). The two-fold reduction in ^{10}Be concentration from EG10-13 to EG10-14 is not explainable by

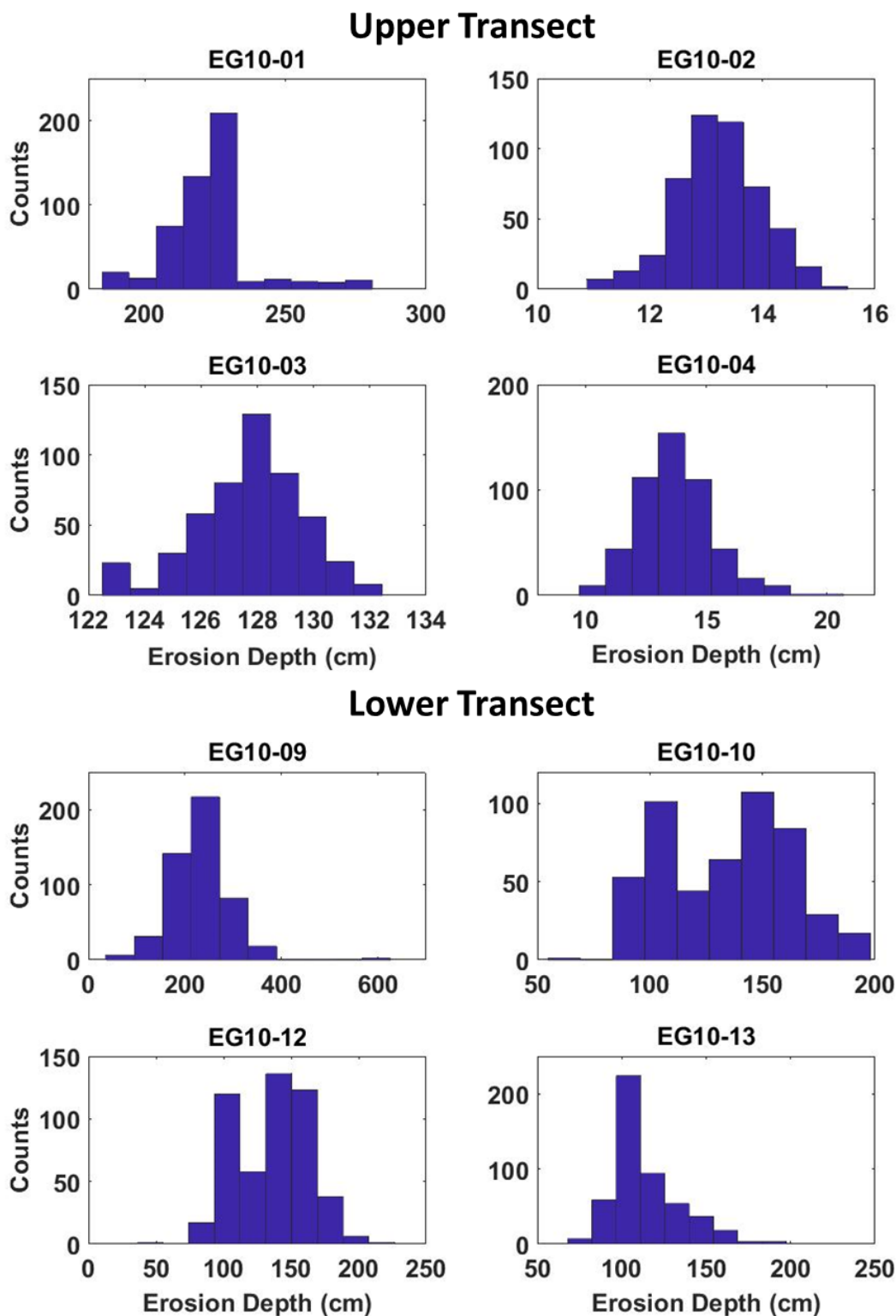


Figure 2.4. Histograms showing the results of the 500-point Monte Carlo bootstrapping calculation done to determine the errors on our erosion depth calculations. Note the flatter distribution of lower transect results and in particular the non-normal distributions for samples EG10-10 and EG10-12, indicating our lower confidence in erosion depths for the lower transect.

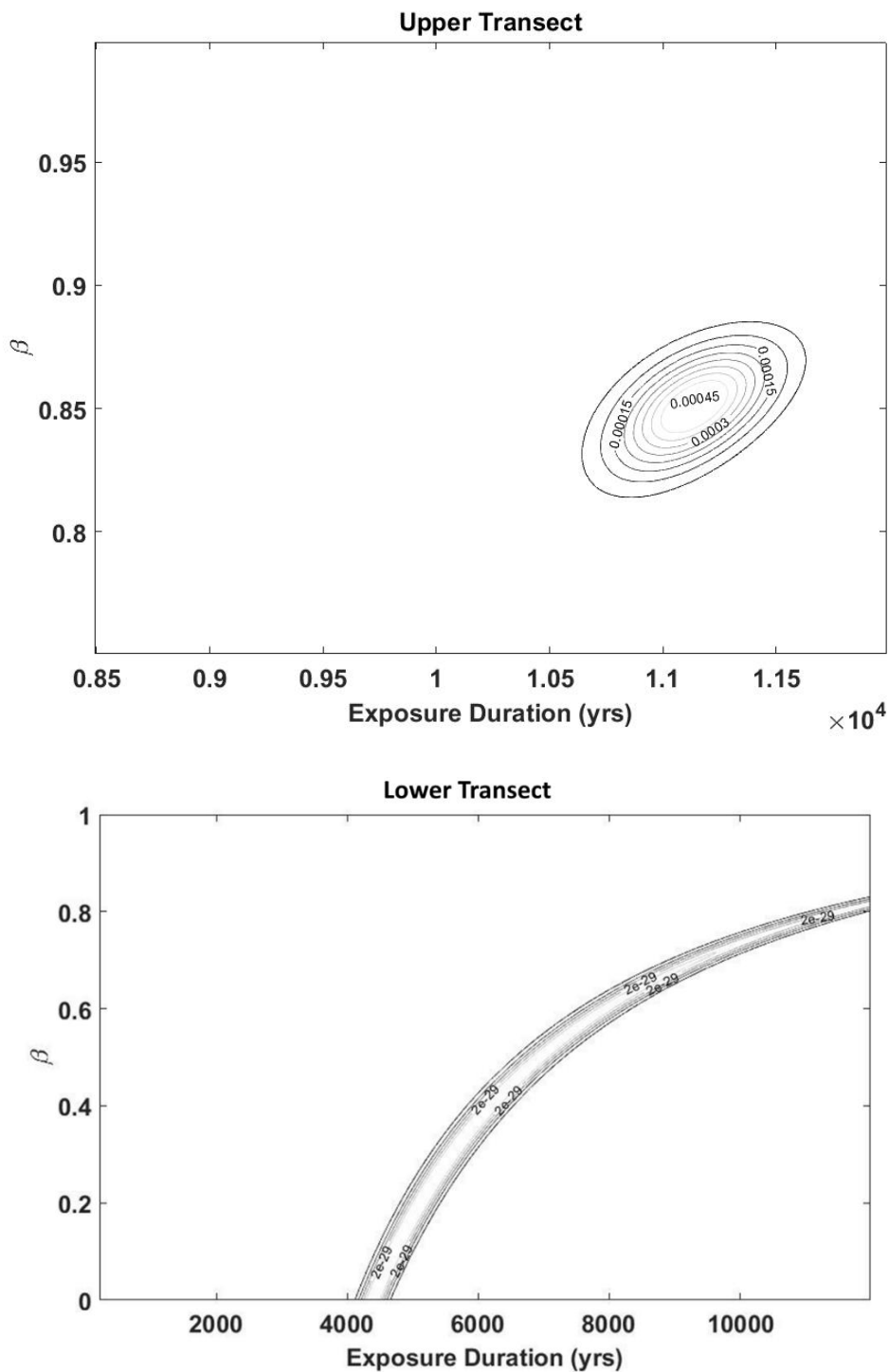


Figure 2.5. Contour plots of the joint probability densities of t_e and β for our upper and lower transects. Note the much broader range of possible exposure durations for the lower transect as opposed to the upper. Also note the lower probable β values for the lower transect compared to the upper, as expected given the lower elevation of the lower transect. These plots assume $T_0 = 12$ ka, based on Olsen (2002).

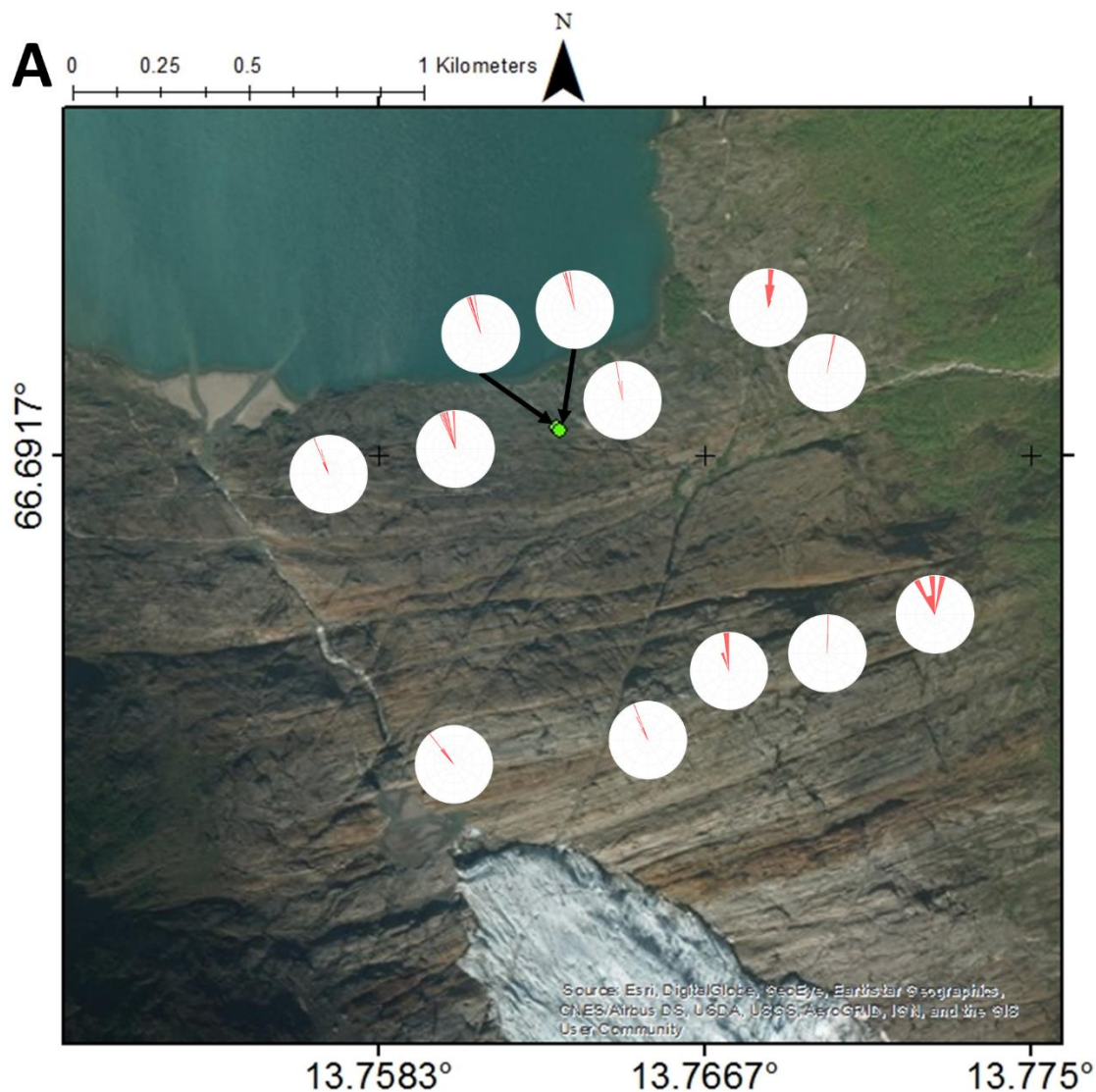


Figure 2.6. Striation trend and foliation strike and dip data from our study site. **A:** Aerial photograph of our study site (courtesy of Esri) with rose diagrams of the trends of glacial striations near individual sample locations overlaid. As one approaches the right lateral margin of the glacier forefield from the center of the valley, the striae are oriented more easterly, parallel to the edge of the valley. Photographs of Engabreen in a more extended state (e.g., Fig. 1.5) show that it extended more along the eastern edge of the valley, confirming these results. **(Continued on next page)**

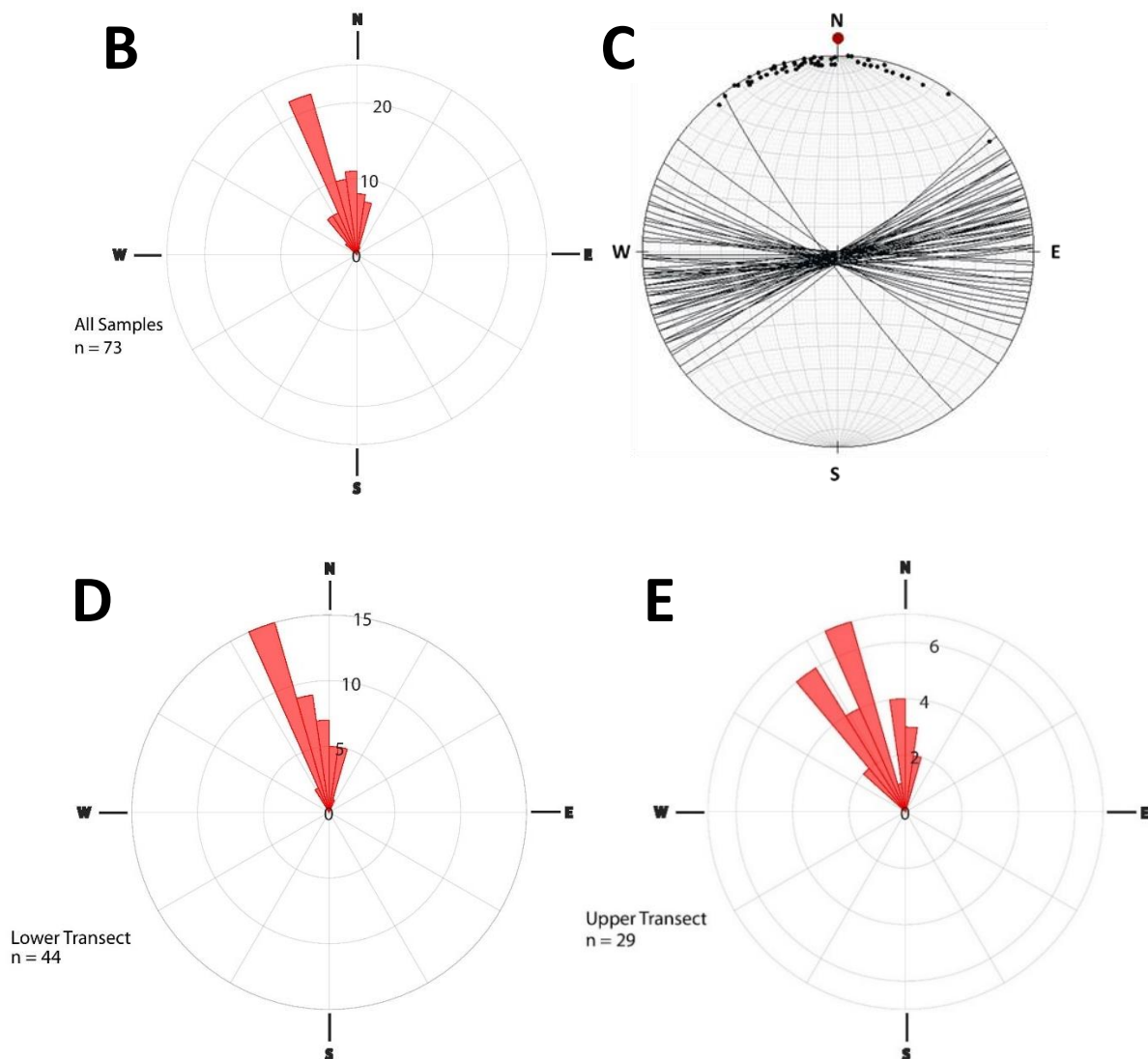


Figure 2.6 (continued). **B:** Rose diagram aggregating all striae trends displayed in Fig. 2.6A ($n = 73$). The dominant striation direction is parallel to ice flow with a weaker signal showing more northerly trend, consistent with past flow along the eastern valley wall. **C:** Stereonet displaying strike and dip of foliations measured within our study area ($n = 59$). Poles (circles) corresponding to measured planes (lines) are displayed as well. Bedrock foliation in the study area is vertical to subvertical and dominantly east-west trending, perpendicular to ice flow. **D:** Rose diagram aggregating striae trends observed along the lower transect in Fig. 2.6A ($n = 44$). Lower transect striae show the same dominant flow-parallel trend as the larger dataset but show a relatively stronger northward signal consistent with greater flow along the eastern valley edge at lower elevations. **E:** Rose diagram aggregating striae trends observed along the upper transect in Fig. 2.6A ($n = 29$). Being closer to the ice front, this dataset displays a stronger flow-parallel trend.

the increased topographic shielding at site EG10-14 relative to site EG10-13. Rather, the vertical surface from which EG10-14 was collected likely represents a plucked face and the ^{10}Be concentration in EG10-14 production at a greater depth.

Another puzzling aspect of this variation is the lower ^{10}Be concentrations observed among the lower transect samples relative to those of the upper transect. This has particular relevance given our method, as we obtain different results by calculating the exposure duration of each transect separately. When we do so, we calculate 6.9 ± 0.2 kyr of exposure for the lower transect and 11.1 ± 0.2 kyr of exposure for the upper transect. This is precisely the opposite of the geomorphic expectation, which would predict less exposure for the higher elevation upper transect. While it is possible that our mathematical method breaks down at high erosion rates, an alternative possibility is presented by examining the Holocene marine limit in Norway. Figure 2.7 shows samples from our lower transect would likely have been underwater for a portion of the time they were exposed (specifically, when they were not covered by the glacier), which would explain the low calculated exposure duration. While our method is unable to discriminate between coverage by water and ice, the fact that our upper transect was mostly above the marine limit allows us to estimate that the additional ~ 5 kyr of burial experienced by the lower transect is due to inundation (Høgaas *et al.*, 2012). Exact calculation of the ratio of the duration of burial by water versus by ice would require multiple pairs of nuclides and analytical accuracy sufficient to detect the slight change in density between ice and liquid water.

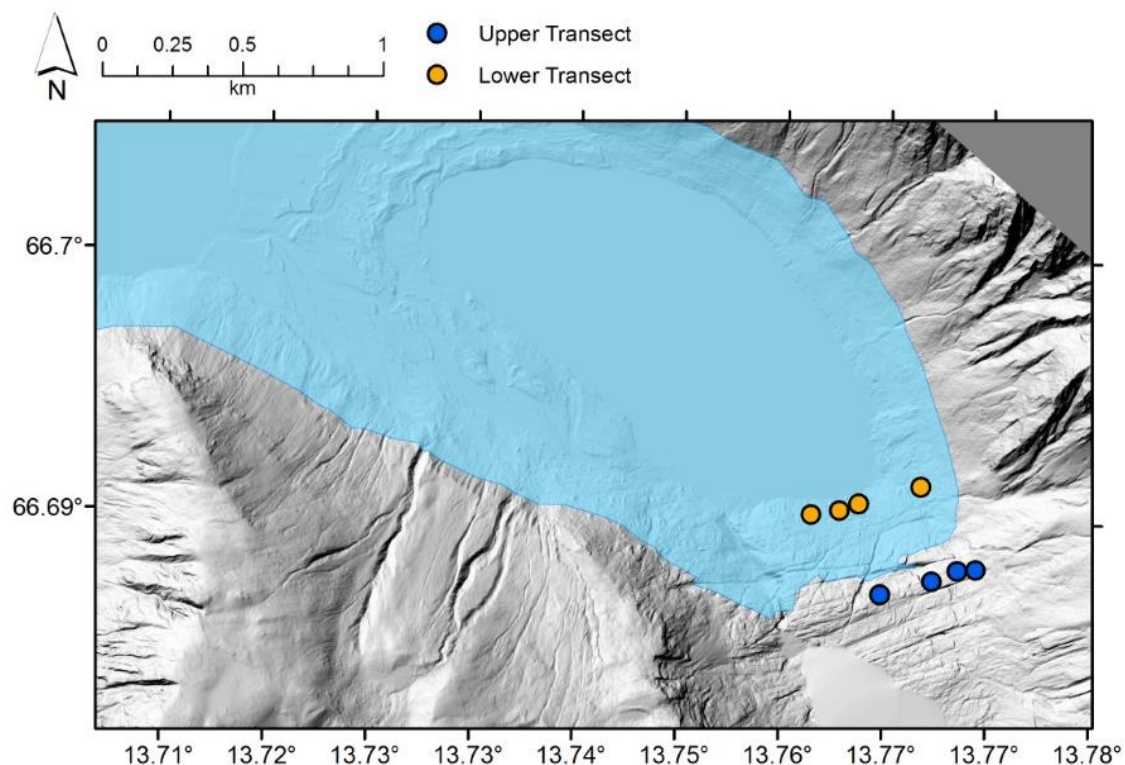


Figure 2.7. Map showing the Holocene marine limit overlain across LiDAR data depicting our study site. Areas below the marine limit (i.e., areas which would have been inundated at some point since deglaciation) are shaded blue, areas above the marine limit are shaded grey. Sample locations are marked with circles, orange for the lower transect and blue for the upper transect. All of the lower transect samples would have been covered by water at peak sea levels, which may account for the lower calculated exposure duration for the lower transect relative to that of the upper transect. Elevation and marine limit data from Norges geologiske undersøkelse, based on Høgaas *et al* (2012).

A third noteworthy aspect of our results is the range of ^{14}C - ^{10}Be concentration ratios exhibited, in particular the samples with ratios exceeding the ^{14}C - ^{10}Be production rate ratio. While it is possible that measurement or sample preparation errors account for these results, we suspect that the results are accurate because the predicted ^{14}C - ^{10}Be concentration ratio increases with depth (Heisinger *et al.*, 2002a, 2002b), as do the ratios we observe in our results (Fig. 2.8).

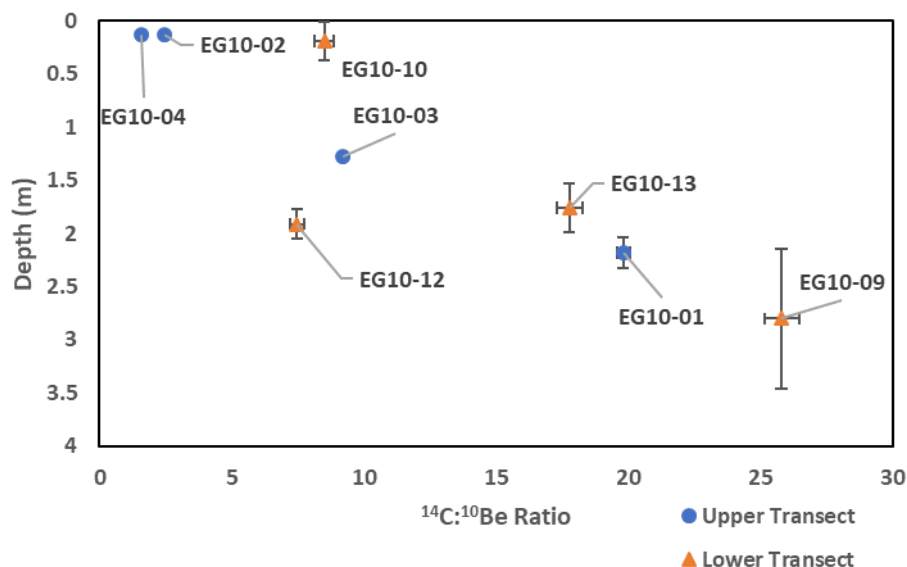


Fig. 2.8. ^{14}C - ^{10}Be ratios of samples from the upper (blue circles) and lower (orange triangles) transects. The shallowly eroded samples of the upper transect (EG10-02 and EG10-04) have the lowest ratios and these ratios decrease with depth, demonstrating the reduced attenuation of in situ ^{14}C production with depth relative to that of ^{10}Be .

2.6.2 Glacial Erosion

The classical model of glacial abrasion predicts that the drag from valley walls decreases the sliding speed and, therefore, the abrasion rate, of a glacier towards its lateral edges (Hallet, 1979). Additionally, the overburden of ice increases the force exerted by tools (such as plucked rock fragments embedded in basal ice) on the bed of a glacier (Hallet, 1981). We expect, therefore, that abrasion rates at our site will correlate with distance from the valley walls and increase towards local topographic lows. Erosion depths calculated for our sample sites, however, correlate with neither relative elevation within each transect nor distance from the valley walls (Table 2.3, Fig. 2.9). This ideal model of glacial erosion does not, at first glance, adequately describe our study site; the adjacency of deeply and shallowly eroded samples and lack of spatial trends (Fig. 2.10) indicate that localized plucking (or abrasion) of a magnitude

much greater than that of abrasion dominates erosion at our site. We interpret the lack of spatial trend in nuclide concentrations at our site as evidence that this localized plucking has occurred, removing blocks of bedrock in which in situ cosmogenic nuclides were concentrated and exposing rock with lower concentrations. If the plucked faces are themselves striated, it is likely that the plucking occurred before the recent extension in historical times (Worsley, 1974). The absence of striae on plucked faces as well as evidence from nuclide concentrations that we will discuss below leads us to believe that the plucking at our sample sites was, in fact, recent.

Additionally, the scenario discussed above explains the anomalously high ^{14}C - ^{10}Be concentration ratios observed in our lower transect (Fig. 2.11). The loss of rock material containing mostly spallation products from the lower transect could explain the preferential decrease in ^{10}Be concentration from the upper to the lower transect relative to that of ^{14}C . Figure 2.12 illustrates the production rate depth dependence of ^{14}C as a function of ^{10}Be production. Observe that, for the lower transect (with the lower β), ^{14}C production is less attenuated with depth relative to ^{10}Be production. Thus, as surface rock is removed from the surface of the two transects by erosion, the ^{14}C - ^{10}Be concentration ratio of the lower transect will increase at a faster rate than will that of the upper transect. The higher overall erosion rates calculated for the lower transect may therefore be related to overdeepening associated with the excavation of Engabreevatnet.

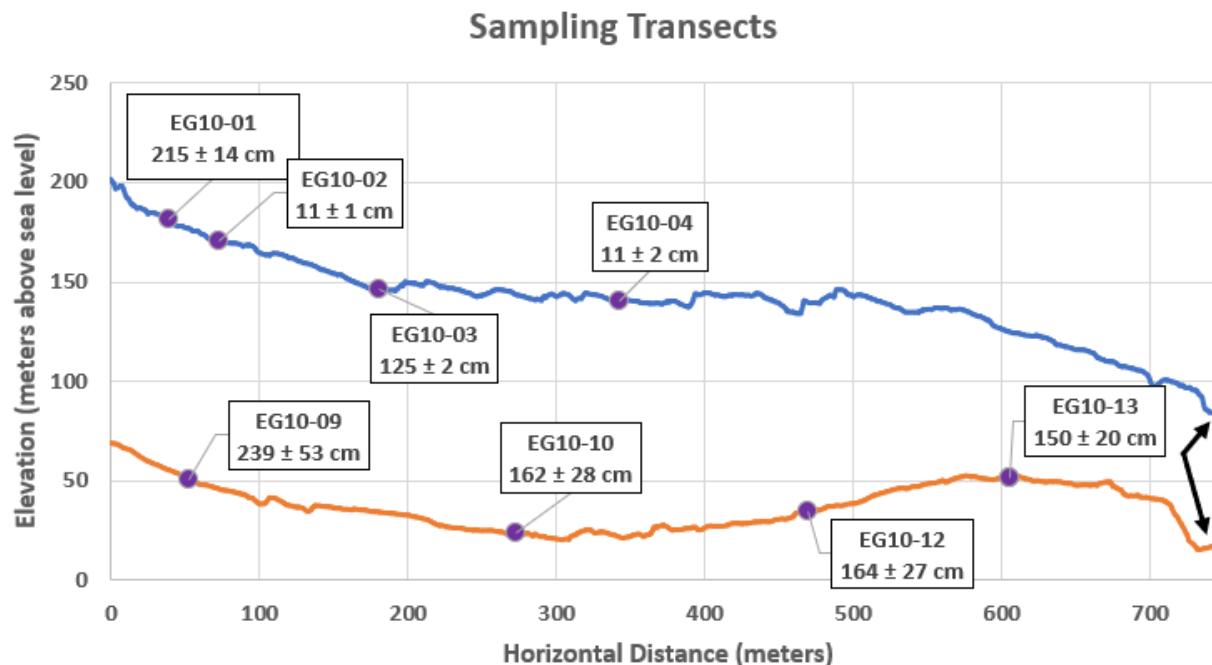


Fig. 2.9. Elevation profiles of our two sampling transects. Sample sites (purple circles) are shown projected onto the upper (blue line) and lower (orange line) transects. The y-axis corresponds to the eastern valley wall (you are looking upvalley in this figure). Samples are labeled with their sample name. Note that, as the ^{14}C concentration in sample EG10-14 was not measured, that sample is not displayed here. The main Nye channel carrying meltwater out from below Engabreen along the right-lateral wall of the valley is denoted with a black arrow. It is evident from this data that proximity to the valley wall and elevation are not the primary controls on erosion depths (nor, therefore, erosion rates) which vary significantly even between nearby samples. The great changes between nearby samples indicates localized plucking, present at the heavily eroded but not the shallowly eroded sites, is a significant erosive process at Engabreen. Elevation data from the Norwegian Mapping Authority.

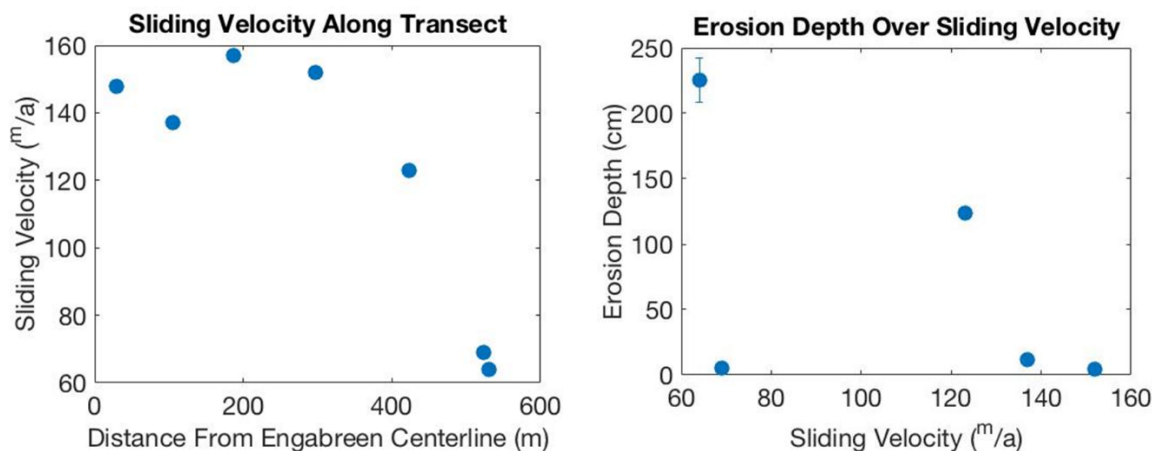
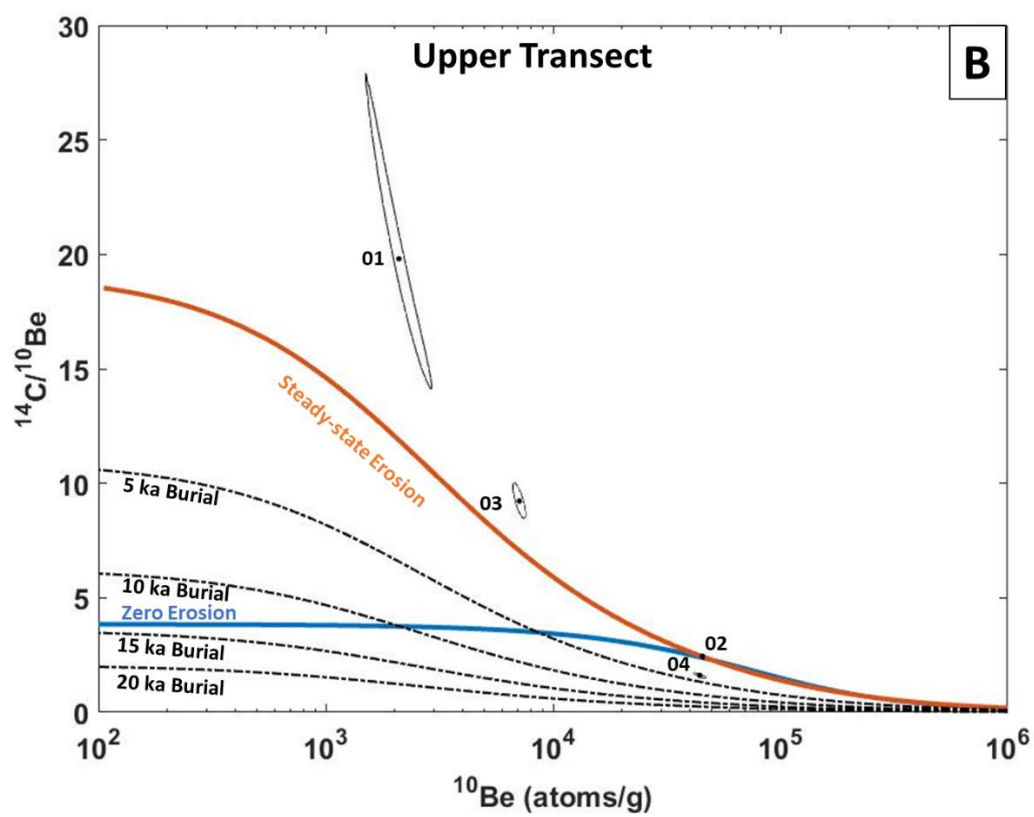
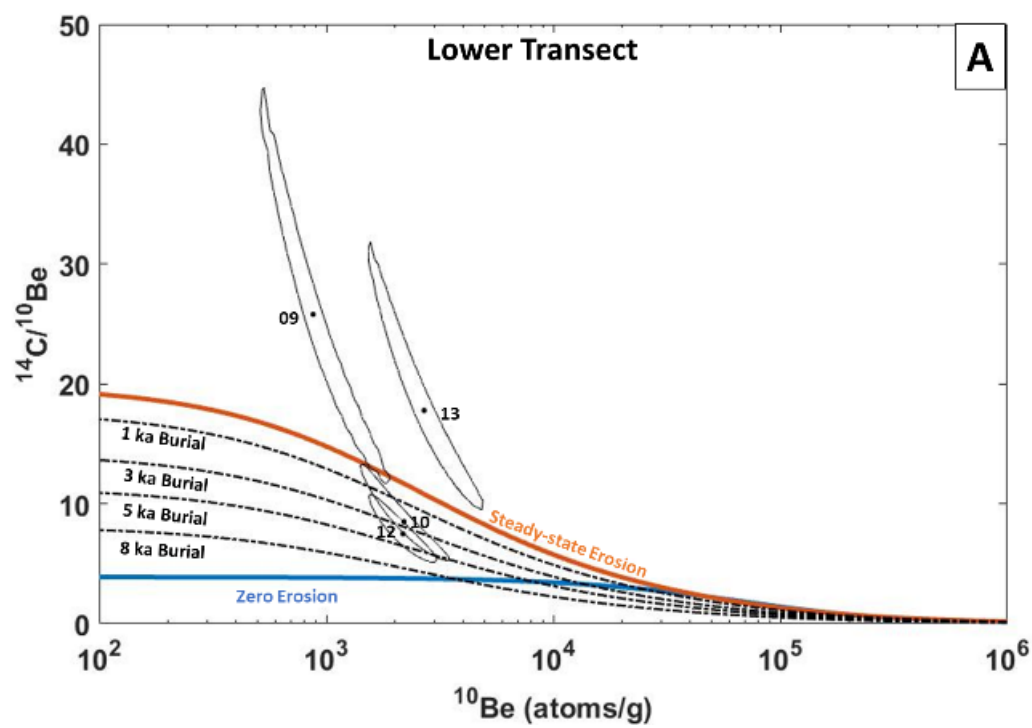


Figure 2.10. Sliding velocity and erosion depth calculated at sample sites of our upper transect. **(Left)** Sliding velocity as predicted by the method of Nye (1952), which takes drag from valley walls and floor into account when calculating basal sliding velocity. We calculated these velocities given the surface velocities reported for the Engabreen terminus in Jackson *et al.* (2005). The plot here shows the expected quadratic dropoff in velocity due to drag from the valley walls. The maximum velocity is offset from the centerline due to the topographic asymmetry of Engabreen. **(Right)** Erosion depths calculated for samples from our upper transect plotted over calculated surface velocity at the sample site. Were abrasion the main control on erosion at Engabreen, sliding velocity (i.e., erosive power) would correlate with erosion depth and this data would show a positive trend. The lack of such a trend indicates that processes other than abrasion are exerting a control on the distribution and magnitude of erosion at Engabreen.

Figure 2.11 (next page). Lal-Klein-Nishiizumi C-Be plots. Individual samples (black circles) are superimposed on curves: those of “zero erosion” (blue), “steady-state erosion” (orange), and several burial isochrons (black). Error ellipses denote 68% sample concentration uncertainties and illustrate the covariance of said. Samples are labeled by name. “EG10-” has been omitted from all labels in this figure for brevity. Note that, as the ^{14}C concentration in sample EG10-14 was not measured, that sample is not displayed here. **A:** Lower transect samples. Two of our samples (EG10-10 and EG10-12) plot in the “steady-state erosion window” between the two curves around the 3 ka burial isochron and two (EG10-09 and EG10-13) in the “forbidden zone”, the area of the plot in which the ^{14}C - ^{10}Be concentration ratio exceeds that predicted by the ^{14}C - ^{10}Be surface production rate ratio for a given ^{10}Be concentration. The two “steady-state erosion window” samples indicate short burial durations at high erosion rates but the two “forbidden zone” samples indicate even higher erosion rates sufficient to expose rock in which the attenuation of production by spallation reactions is great enough to significantly alter the production ratio of the two nuclides. Note that, as the ^{14}C concentration was not measured in sample EG10-14, it is not plotted here. **B:** Upper transect samples. Note that these samples show generally greater ^{10}Be concentrations than do lower transect samples. Two of these samples (EG10-01 and EG10-03) plot in the “forbidden zone” indicating high erosion rates. The 68% confidence ellipses of both remaining samples are encompassed in (EG10-04) or pass into (EG10-02) the “burial zone” which indicates that their exposure history may be complex. The greater ^{10}Be concentrations of these samples relative to other samples from the upper transect indicates decreased erosion rates assuming that all samples from the transect have similar exposure histories.



2.6.3 Striations and Geomorphic Data

Striations record the dominant direction of ice flow over the burial duration of a bedrock surface, so the more easterly trend of striations along the lower transect agrees with historical imagery showing that Engabreen flowed along the eastern wall of the valley in its more extended state (Fig. 1.5). This path also explains the elevation profile of the lower transect (Fig. 2.2), which exhibits low elevations near the valley wall and rises toward the middle of the valley. Visually as well, the lower eastern edge of the valley shows a more concave profile (Fig. 1.4) congruent with enhanced erosion in that area due to greater ice flow.

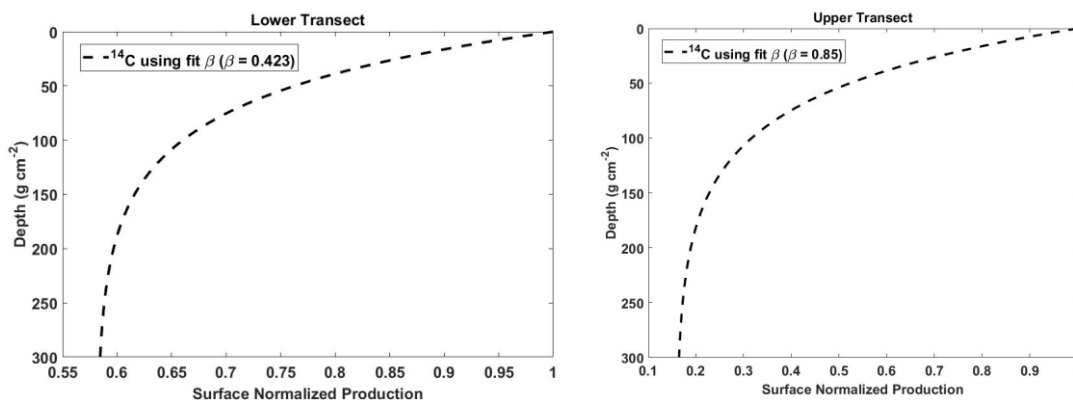


Figure 2.12. ^{14}C production profiles for our upper and lower transects. Production rates (dashed lines) are shown normalized to the surface production rate. Note that, for our lower transect ($\beta = 0.42$), production with depth is attenuated less rapidly than for our upper transect ($\beta = 0.85$). The lower transect is at a lower elevation (i.e. there is a thicker atmosphere above it), so the muon flux is proportionally greater there than at our upper transect because spallation reactions are more attenuated by the time they reach the lower transect. As production by muons dominates production beyond depths of ~ 2.5 m (Briner *et al.*, 2016), samples from the deeply eroded lower transect represent rock in which ^{14}C production is proportionally greater than at higher elevations.

2.7 Conclusions

The in situ nuclide concentrations of our samples make clear that our sample site was uncovered for 11.0 ± 0.2 kyr following deglaciation at the end of the Pleistocene. This indicates that the burial duration of our samples (by Engabreen) was less than a millennium during the Holocene. A short period of burial implies that the erosive subglacial processes recorded in the bedrock of our sample sites occurred rapidly.

Ideal models of glacial flow predict that drag from surfaces such as the valley walls and floor slow ice flow exponentially as one approaches them. If erosion is controlled mainly by the speed at which the glacier flows (and, therefore, the power with which embedded clasts are scraped across the substrate), one should expect the deepest erosion to occur near the center of a valley, the furthest point from the valley walls. Even accounting for the topographic asymmetry of the valley down which Engabreen flows, it is clear that flow velocity is not the dominant control on subglacial erosive activity here. Plucking in particular seems to depend on local conditions much more than valley-scale inputs.

Extremely low in situ concentrations in a sample compared to those of samples from neighboring sites likely indicate recent plucking which would have suddenly exposed previously deeply buried surfaces.

The integrated exposure duration of our transects implies that ice cover during the Holocene at this site was minimal. Much of the burial duration may have occurred in the recent, even historical past (Worsley, 1974; Worsley and Alexander, 1976). The high ^{14}C - ^{10}Be concentration

ratios in samples indicates that the plucking and subsequent reabrasion at our sites occurred during recent cover as it has not yet been overprinted by production at surficial rates.

Appendices A: Site Images



Figure A.1. Eastward view along the bedrock ridge along which our upper transect runs. Engabreen is behind the photographer in this photograph. Photo courtesy of Dr. Brent Goehring.



Figure A.2. Example of a plucked face (highlighted by a black oval) from the lower transect. Boot for scale. The top of this image is uphill.



Figure A.3. Example of a crescentic gouge filled with rainwater from site EG10-13 (on the lower transect). The curved face of the gouge bows downhill. Boot for scale.



Figure A.4. Example of a plucked face near site EG10-06 (on the upper transect). Boot for scale.

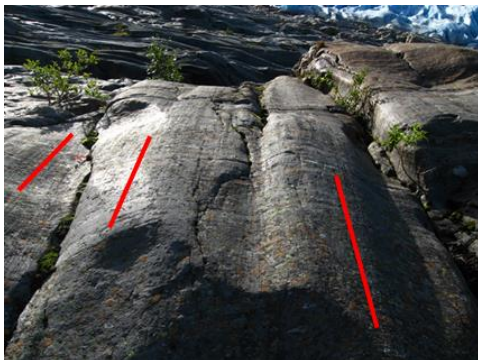


Figure A.5. Southward (uphill) view from the upper transect towards the Engabreen ice front. Note the polished, striated surface of the exposed bedrock (several striations mapped by red lines). Photo courtesy of Dr. Brent M. Goehring.

Table A.1

Sample Images



	<p>EG10-01</p> <p>Upper Transect</p> <p>181 m a.s.l.</p>
	<p>EG10-02</p> <p>Upper Transect</p> <p>168 m a.s.l.</p>

Table A.1 (continued)

Sample Images


	<p>EG10-03</p> <p>Upper Transect</p> <p>155 m a.s.l.</p>
	<p>EG10-04</p> <p>Upper Transect</p> <p>146 m a.s.l.</p>

Table A.1 (continued)

Sample Images


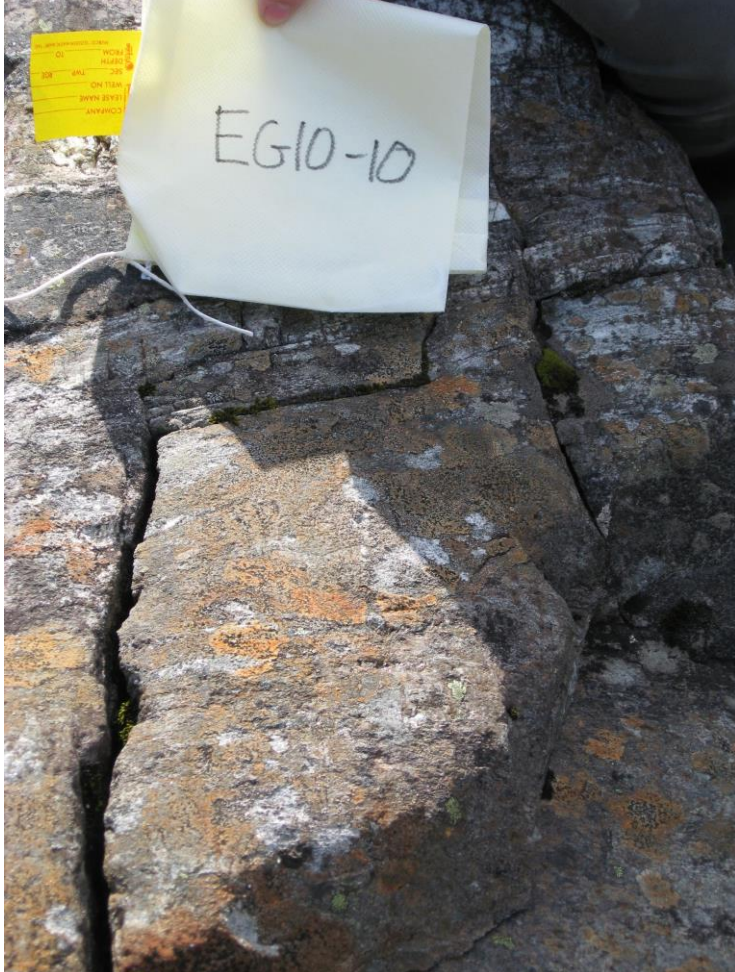
	<p>EG10-09</p> <p>Lower Transect</p> <p>27 m a.s.l.</p>
	<p>EG10-10</p> <p>Lower Transect</p> <p>20 m a.s.l.</p>

Table A.1 (continued)

Sample Images


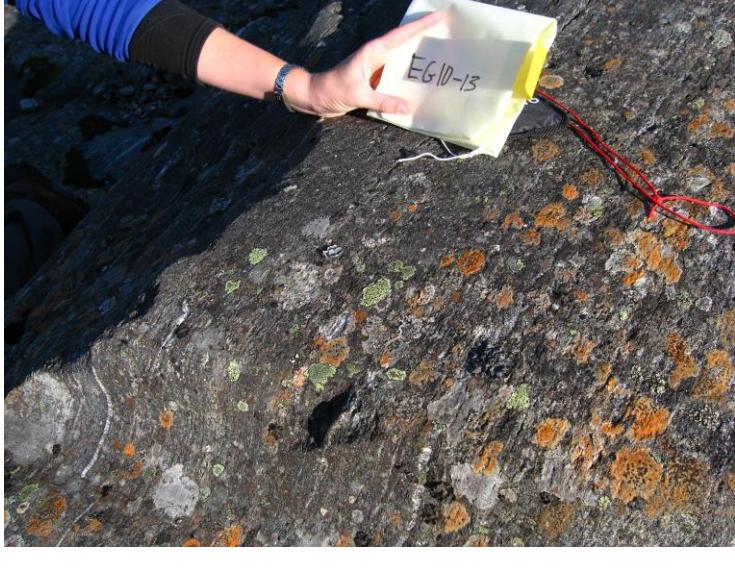

	<p>EG10-12</p> <p>Lower Transect</p> <p>24 m a.s.l.</p>
	<p>EG10-13</p> <p>Lower Transect</p> <p>32 m a.s.l.</p> <p>(Note: this sample was collected from the stoss face of the same bedform as EG10-14)</p>

Table A.1 (continued)

Sample Images

	<p>EG10-14</p> <p>Lower Transect</p> <p>32 m a.s.l.</p> <p>(Note: this sample was collected from the lee face of the same bedform as EG10-13)</p>
--	---

All photos courtesy of Dr. Brent M. Goehring

Appendix B: Laboratory Methods

B.1 ^{10}Be Extraction Methods

The ^{10}Be fractions were dissolved in concentrated HF (at a ratio of 5 ml HF:1 g quartz) and HNO_3 (at a ratio of 1 ml HNO_3 :1 g quartz). Drying the samples down with the addition of concentrated HCl left the sample aliquots as chloride salts. These salts were suitable targets for anion exchange chemistry. We used HCl of varying concentrations to flush the samples through AG 1-X8 Resin (100-200 mesh, chloride form to separate the Be, Ti, and Al fractions from the unwanted Fe fraction. These fractions were then converted to sulfates by drying them down in the presence of H_2SO_4 . Flushing the Be/Al fractions through DOWEX-50 X8 200-400# resin separated the three major cations. We continued to work with the Be fraction.

After the cation exchange chemistry, we added 30% NH_4OH to the Be fractions and centrifuged them to precipitate the Be as $\text{Be}(\text{OH})_2$. Calcination occurred in a tube furnace, which converted the samples to BeO . The samples were then mixed with Nb for loading into cathodes for accelerator mass spectrometer (AMS) analysis.

At the Purdue Rare Isotope Measurement Laboratory (PRIME Lab), the sample was bombarded with cesium ions to cause it to emit negatively charged ions. These ions were then focused into a beam and accelerated through gas or foil strippers to convert it to a beam of positively charged ions. A magnetic field then deflected the ions according to their mass into detectors positioned at different angles to count specific isotopes (Elmore *et al.*, 1992). The ^{10}Be - ^9Be ratio reported by PRIME Lab utilizes the 07KNSTD standard, with a ^{10}Be - ^9Be concentration ratio of $2.79 \pm 0.03\text{e-}11$ (Nishiizumi *et al.*, 2007).

B.2 ^{14}C Extraction Methods

We extracted in situ ^{14}C from the purified quartz from our samples at the Tulane University Cosmogenic Nuclide Lab (TUCNL) using a method similar to that of Goehring *et al.* (2019), in which the sample is fused in LiBO_2 and released C-species oxidized in O_2 to form CO_2 , which is then purified and graphitized in H_2 in the presence of Fe. We then sent graphitized samples to the National Ocean Sciences Accelerator Mass Spectrometry (NOSAMS) facility for AMS. NOSAMS reports the ^{14}C - ^{12}C ratios of samples relative to the Ox-II standard that we make at TUCNL, which is calibrated to that of the National Bureau of Standards' Oxalic Acid I (NIST SRM 4990) (NOSAMS, 2018).

Appendix C: Bayesian Isochron-fitting Method

Using the method developed in Goehring *et al.* (2013), we determine the probability distributions for t_e and β for all of our samples. The technique is a modified form of Bayes' Theorem (d'Agostini, 2003; Muzikar, 2011) in which we define the probability densities for t_e and β in terms of the probability distribution of our data:

$$P(t_e, \beta | data) P(data) = P(data | t_e, \beta) P_0(t_e, \beta) \quad (C.1)$$

in which $P(t_e, \beta | data)$ refers to the joint probability-density function for t_e and β given our data (^{10}Be and ^{14}C concentrations and production rates). Calculating this result is our objective. $P(data)$ is the prior probability of obtaining said data. $P(data | t_e, \beta)$ refers to the probability function of our data given t_e and β values. $P_0(t_e, \beta)$ represents the prior constraints on t_e and β . Essentially, this term excises impossible results (i.e. exposure durations greater than the time elapsed since the samples were first exposed) from the function.

We then define a variable c such that

$$\int dt_e \int d\beta P(t_e, \beta | data) = 1. \quad (C.2)$$

In other words, the cumulative probabilities of t_e and β must sum to 1. This variable allows us to write Eq. (7) as

$$P(t_e, \beta | data) = c P(data | t_e, \beta) P_0(t_e, \beta). \quad (C.3)$$

We must then define two additional variables: G_i and H . G_i is the Gaussian probability distribution for a given sample i and is defined as

$$G_i = e^{\frac{-(N_{14i} - P_{14i}) \left[(1 - \beta) + \frac{\beta N_{10i}}{2\sigma_{14i}^2} \right] \left[e^{\lambda_{14} t_e - 1} \right] e^{-\lambda_{14} [T_0 - t_e]} \right)^2}{2\lambda_{14} \sigma_{14i}^2}}. \quad (C.4)$$

H is a step function which we use to exclude impossible results from our calculations. It is defined such that

$$H\left(t_e - \frac{N_{10i}}{P_{10i}}\right) = \begin{cases} 0, & t_e - \frac{N_{10i}}{P_{10i}} < 0 \\ 1, & t_e - \frac{N_{10i}}{P_{10i}} > 0 \end{cases} \quad (C.5)$$

It works by treating the naïve exposure age ($\frac{N_{10,i}}{P_{10,i}}$) of the sample with the youngest apparent exposure age as the lower limit of the exposure duration of the samples as each sample must have been exposed for at least as long as the least exposed sample was. This assumption is of course only true for the lower limit of exposure – the same assumption cannot be made for the upper limit as erosion and radioactive decay could cause the apparent oldest sample to display an age younger than its true exposure duration. $H = 0$ for exposure durations that are too short or too long to produce the observed results. This ensures that our equation for $P(data|t_e, \beta)$,

$$P(data|t_e, \beta) = (\prod_i G_i)(\prod_i H(t_e - \frac{N_{10i}}{P_{10i}})) \quad (C.6)$$

in which $\prod_i G_i$ and $\prod_i H$ represent the products of the G_i and H matrices for each sample, respectively, will return zero likelihood for any impossible values of t_e . We can then calculate the joint probability distribution for any pair of t_e and β value using the following equation:

$$P(t_e, \beta|data) = c (\prod_i G_i) H(t_e - LL) P_0(t_e, \beta), \quad (C.7)$$

in which LL stands for the lower limit of possible t_e values for our dataset. Eq. (13) then allows us to calculate the PDF of β as

$$P(\beta) = \int_{LL}^{T_0} P(t_e, \beta|data) dt_e \quad (C.8)$$

and the average value of β as

$$\langle \beta \rangle = \int_0^1 P(\beta) d\beta. \quad (C.9)$$

We then calculate the uncertainty on β , therefore, as

$$\sigma^2 = \int_0^1 (\beta - \langle \beta \rangle)^2 P(\beta) d\beta. \quad (C.10)$$

We calculate the PDF, average value, and uncertainty of t_e by simply swapping t_e and β in Eqs. (14-16) and changing to the associated limits of integration. The burial duration of our samples was calculated by subtracting the most likely t_e value from T_0 , treating any time spent not exposed as time spent covered.

Appendix D: Geochemical Data Tables

Table D.1.

¹⁴C Sample Geochemical Data

Sample ID	Quartz Mass (g)	Carbon Yield (μg)	±1σ (μg)	Diluted Carbon Mass (μg)	±1σ (μg)	¹⁴C/total Carbon	±1σ	[¹⁴C][†] (atoms g⁻¹)	±1σ (atoms g⁻¹)
EG10-01	4.9909	472.7	6.1	472.7	6.1	1.15e-14	2.55e-14	4.16e+4	1.54e+3
EG10-02	10.1817	399.0	1.2	386.6	4.6	6.64e-14	13.16e-14	10.99e+4	3.72e+3
EG10-03	7.9905	517.0	1.3	387.2	4.7	3.71e-14	7.30e-14	6.44e+4	3.46e+3
EG10-04	4.5368	15.6	0.2	110.1	1.4	7.01e-14	5.87e-14	7.11e+4	1.86e+3
EG10-09	4.6723	10.2	0.1	105.7	1.4	3.22e-14	3.45e-14	2.26e+4	1.54e+3
EG10-10	4.8203	6.4	0.1	107.5	1.4	2.88e-14	3.84e-14	1.87e+4	1.48e+3
EG10-12	4.7523	14.2	0.2	108.7	1.4	2.61e-14	3.64e-14	1.63e+4	1.49e+3
EG10-13	2.0525	9.7	0.1	111.0	1.4	2.93e-14	3.69e-14	4.80e+4	3.49e+3

[†]¹⁴C concentration

Process Blanks

Sample Blank	Effective Blank (atoms)	±1σ (atoms)
EG10-01 and 04-13	9.51e+4	8.94e+3
EG10-02 and 03	27.1e+4	10.5e+3

Table D.2.¹⁰Be Sample Geochemical Data

Sample ID	Quartz Mass (g)	Be Carrier ($\mu\text{g Be}$)	¹⁰ Be/ ⁹ Be	$\pm 1\sigma$	[¹⁰ Be] [†] (atoms g ⁻¹)	$\pm 1\sigma$ (atoms g ⁻¹)
EG10-01	25.5337	0.2704	4.02e-15	6.24e-16	2.10e+3	4.96e+2
EG10-02	-	-	-	-	45.4e+3	6.81e+2
EG10-03	-	-	-	-	7.11e+3	3.06e+2
EG10-04	33.9257	0.2709	83.8e-15	3.23e-16	44.2e+3	17.9e+2
EG10-09	25.0174	0.2695	2.28e-15	7.32e-16	0.876e+3	5.75e+2
EG10-10	26.3137	0.2686	4.29e-15	10.3e-16	2.20e+3	7.39e+2
EG10-12	25.0792	0.2687	4.11e-15	6.50e-16	2.18e+3	5.20e+2
EG10-13	12.8050	0.2690	2.99e-15	8.41e-16	2.70e+3	12.6e+2

Process Blanks

Sample Blank	Be Carrier ($\mu\text{g Be}$)	¹⁰ Be/ ⁹ Be	$\pm 1\sigma$	[¹⁰ Be] [†] (atoms g ⁻¹)	$\pm 1\sigma$ (atoms g ⁻¹)
EG10-01 and 04-13	0.26936	1.06e-15	3.20e-16	1.91e+4	57.5e+2
EG10-02 and 03	-	-	-	4.50e+4	6.81e+2

[†]¹⁰Be concentration

List of References

- Nesje, A., Latest Pleistocene and Holocene alpine glacier fluctuations in Scandinavia, *Quaternary Science Reviews* (2009). doi:10.1016/i.quascirev.2008.12.016
- Koppes, Michéle, et al. "Observed latitudinal variations in erosion as a function of glacier dynamics." *Nature* 526.7571 (2015): 100-103.
- Hallet, Bernard, Lewis Hunter, and Jim Bogen. "Rates of erosion and sediment evacuation by glaciers: A review of field data and their implications." *Global and Planetary Change* 12.1-4 (1996): 213-235.
- Balco, Greg. "Contributions and unrealized potential contributions of cosmogenic-nuclide exposure dating to glacier chronology, 1990–2010." *Quaternary Science Reviews* 30.1-2 (2011): 3-27.
- Davis, P. Thompson, Brian Menounos, and Gerald Osborn. "Holocene and latest Pleistocene alpine glacier fluctuations: a global perspective." *Quaternary Science Reviews* 28.21-22 (2009): 2021-2033.
- Martini, Ireneo Peter, Michael E. Brookfield, and Steven Sadura. *Principles of glacial geomorphology and geology*. Pearson College Div, 2001.
- Nye, J. F. "The mechanics of glacier flow." *Journal of Glaciology* 2.12 (1952): 82-93.
- Beaud, Flavien, Gwenn E. Flowers, and Jeremy G. Venditti. "Efficacy of bedrock erosion by subglacial water flow." *Earth Surface Dynamics* 4.1 (2016): 125-145.
- Hallet, Bernard. "Glacial abrasion and sliding: their dependence on the debris concentration in basal ice." *Annals of Glaciology* 2 (1981): 23-28.
- Hooyer, Thomas S., Denis Cohen, and Neal R. Iverson. "Control of glacial quarrying by bedrock joints." *Geomorphology* 153 (2012): 91-101.
- Anderson, Robert S. "Evolution of lumpy glacial landscapes." *Geology* 42.8 (2014): 679-682.
- Hallet, Bernard. "A theoretical model of glacial abrasion." *Journal of Glaciology* 23.89 (1979): 39-50.
- Röthlisberger, Hans, and Almut Iken. "Plucking as an effect of water-pressure variations at the glacier bed." *Annals of Glaciology* 2 (1981): 57-62.
- Clayton, Lee, John W. Attig, and David M. Mickelson. "Tunnel channels formed in Wisconsin during the last glaciation." *Special Papers-Geological Society of America* (1999): 69-82.
- Gosse, John C., and Fred M. Phillips. "Terrestrial in situ cosmogenic nuclides: theory and application." *Quaternary Science Reviews* 20.14 (2001): 1475-1560.
- Kennett, Michael, Tron Laumann, and Cecilie Lund. "Helicopter-borne radio-echo sounding of Svartisen, Norway." *Annals of Glaciology* 17.1 (1993): 23-26.
- Cohen, Denis, et al. "Sliding of ice past an obstacle at Engabreen, Norway." *Journal of Glaciology* 46.155 (2000): 599-610.

- Jackson, Miriam, Ian A. Brown, and Hallgeir Elvehøy. "Velocity measurements on Engabreen, Norway." *Annals of glaciology* 42 (2005): 29-34.
- Lappégard, Gaute, and Jack Kohler. "Determination of basal hydraulic systems based on subglacial high-pressure pump experiments." *Annals of Glaciology* 40.1 (2005): 37-42.
- Iverson, Neal R., et al. "Soft-bed experiments beneath Engabreen, Norway: regelation infiltration, basal slip and bed deformation." *Journal of Glaciology* 53.182 (2007): 323-340.
- Messerli, Alexandra. *Surface Velocities and Hydrology at Engabreen: Observations from Feature Tracking and Hydro-Meteorological Measurements*. Diss. The Niels Bohr Institute, Faculty of Science, University of Copenhagen, 2015.
- Karlén, Wibjörn. "Scandinavian glacial and climatic fluctuations during the Holocene." *Quaternary Science Reviews* 7.2 (1988): 199-209.
- Theakstone, W. H. "Recent changes in the glaciers of Svartisen." *Journal of Glaciology* 5.40 (1965): 411-431.
- Bond, Gerard, et al. "A pervasive millennial-scale cycle in North Atlantic Holocene and glacial climates." *science* 278.5341 (1997): 1257-1266.
- Nesje, A., Dahl, S.O., Bakke, J., 2004. Were abrupt Lateglacial and early-Holocene climatic changes in northwest Europe related to freshwater outbursts to the North Atlantic and Arctic oceans? *The Holocene* 14, 299-310.
- Karlén, W., Kuylenstierna, J., 1996. On solar forcing of Holocene climate: evidence from Scandinavia. *The Holocene* 6, 359-365.
- Nesje, A., Bakke, J., Dahl, S.O., Lie, Ø., Matthews, J.A., 2008. Norwegian mountain glaciers in the past, present, and future. *Global and Planetary Change* 60, 10-27.
- Olsen, Lars. "Mid and Late Weichselian, ice-sheet fluctuations northwest of the Svartisen glacier, Nordland, northern Norway." *Geol. Surv. Norway Bull* 440.39-52 (2002).
- Worsley, Peter, and Alexander, Michael J.. "Glacier and environmental changes—Neoglacial data from the outermost moraine ridges at Engabreen, northern Norway." *Geografiska Annaler: Series A, Physical Geography* 58.1-2 (1976): 55-69.
- Winkler, Stefan. "A new interpretation of the date of the 'Little Ice Age' glacier maximum at Svartisen and Okstindan, northern Norway." *The Holocene* 13.1 (2003): 83-95.
- Oerlemans, Johannes. "Extracting a climate signal from 169 glacier records." *science* 308.5722 (2005): 675-677.
- Benn, Douglas, and David JA Evans. *Glaciers and glaciation*. Routledge, 2014.
- Riihimaki, Catherine A., et al. "Sediment evacuation and glacial erosion rates at a small alpine glacier." *Journal of Geophysical Research: Earth Surface* 110.F3 (2005).

- Farber, Daniel L., Anne-Sophie Mériaux, and Robert C. Finkel. "Attenuation length for fast nucleon production of ^{10}Be derived from near-surface production profiles." *Earth and Planetary Science Letters* 274.3-4 (2008): 295-300.
- Briner, Jason P., et al. "The deep accumulation of ^{10}Be at Utsira, southwestern Norway: implications for cosmogenic nuclide exposure dating in peripheral ice sheet landscapes." *Geophysical Research Letters* 43.17 (2016): 9121-9129.
- Nishiizumi, Kunihiko, et al. "Absolute calibration of ^{10}Be AMS standards." *Nuclear Instruments and Methods in Physics Research Section B: Beam Interactions with Materials and Atoms* 258.2 (2007): 403-413.
- Sigmond, E. M. O., M. Gustavson, and D. Roberts. "Bedrock map of Norway, 1: 1 million." *Norges Geologiske Undersøkelse*, Trondheim (1984).
- Theakstone, Wilfred H. "Long-term variations of the seasonal snow cover in Nordland, Norway: the influence of the North Atlantic Oscillation." *Annals of Glaciology* 54.62 (2013): 25-34.
- Andreassen, Liss M., et al. "Modelling the climate sensitivity of Storbreen and Engabreen, Norway." (2006).
- Stroeven, Arjen P., et al. "A new Scandinavian reference ^{10}Be production rate." *Quaternary Geochronology* 29 (2015): 104-115.
- Stone, John O. "Air pressure and cosmogenic isotope production." *Journal of Geophysical Research: Solid Earth* 105.B10 (2000): 23753-23759.
- Goehring, Brent M., Jim Wilson, and Keir Nichols. "A fully automated system for the extraction of in situ cosmogenic carbon-14 in the Tulane University cosmogenic nuclide laboratory." *Nuclear Instruments and Methods in Physics Research Section B: Beam Interactions with Materials and Atoms* (2019).
- Hippe, Kristina, and Nathaniel A. Lifton. "Calculating isotope ratios and nuclide concentrations for In situ cosmogenic ^{14}C analyses." *Radiocarbon* 56.3 (2014): 1167-1174.
- Goehring, Brent M., Paul Muzikar, and Nathaniel A. Lifton. "An in situ ^{14}C - ^{10}Be Bayesian isochron approach for interpreting complex glacial histories." *Quaternary Geochronology* 15 (2013): 61-66.
- Heisinger, B., et al. "Production of selected cosmogenic radionuclides by muons: 1. Fast muons." *Earth and Planetary Science Letters* 200.3-4 (2002a): 345-355.
- Heisinger, B., et al. "Production of selected cosmogenic radionuclides by muons: 2. Capture of negative muons." *Earth and Planetary Science Letters* 200.3-4 (2002b): 357-369.
- Lowell, Thomas V., et al. "Late Holocene expansion of Istorvet ice cap, Liverpool Land, east Greenland." *Quaternary Science Reviews* 63 (2013): 128-140.
- Miller, Gifford H., et al. "Unprecedented recent summer warmth in Arctic Canada." *Geophysical Research Letters* 40.21 (2013): 5745-5751.

- Rekstad, J. "Beretning om en undersøgelse af Svartisen, foretagen I somrene 1890 og 1891." *Archiv for Matematik og Naturvidenskab* 16 (1893): 266-321.
- Høgaas, F., et al. "Database for registrering av marine grense (MG) i Norge." *NGU rapport* (2012).
- Worsley, P. "On the significance of the age of a buried tree stump by Engabreen, Svartisen." *Arbok* (1974).
- Elmore, David, et al. "PRIME lab: A dedicated AMS facility at Purdue University." *Radiocarbon* 34.3 (1992): 447-451.
- NOSAMS. Woods Hole Oceanographic Institution; [updated 2018 January 17; accessed 2018 November 19]. <http://www.whoi.edu/nosams/general-statement-of-14c-procedures>.
- d'Agostini, G. "Fits, and especially linear fits, with errors on both axes, extra variance of the data points and other complications." *arXiv preprint physics/0511182* (2005).
- Muzikar, Paul. "Geological constraints and ^{26}Al – ^{10}Be burial dating isochrons." *Earth Surface Processes and Landforms* 36.7 (2011): 946-952.

Biography

Cari Rand is a geology student at Tulane University whose studies focus on glaciology.